

Black hole superradiance and polarization-dependent bending of light

Alexis D. Plascencia^a and Alfredo Urbano^{b,c}

^a *Institute for Particle Physics Phenomenology, Department of Physics, Durham University,
Durham DH1 3LE, United Kingdom.*

^b *INFN, sezione di Trieste, SISSA, via Bonomea 265, 34136 Trieste, Italy.*

^c *CERN, Theoretical Physics Department, Geneva, Switzerland.*

Abstract

An inhomogeneous pseudo-scalar field configuration behaves like an optically active medium. Consequently, if a light ray passes through an axion cloud surrounding a Kerr black hole, it may experience a polarization-dependent bending. We explore the size and relevance of such effect considering both the QCD axion and a generic axion-like particle.

Contents

1	Motivation	3
2	Axion clouds around rotating black holes	7
3	Polarization-dependent bending of light	15
3.1	The QCD axion	18
3.2	The photo-philic QCD axion	20
3.3	Axion-like particles	22
4	Discussion and outlook	23
4.1	General remarks: dual-polarization receiver and VLBI	23
4.2	Comparison with “background” effects	25
4.3	Faraday rotation	27
5	Conclusions	28
A	Radial eigenfunctions and rotating axion cloud	29
B	Modified dispersion relation	30
C	Equation for the photon orbit	33

1 Motivation

Superradiance is a radiation enhancement process which occurs in the presence of a dissipative system. We refer the interested reader to [1] for an excellent and comprehensive review about the role of superradiance in astrophysics and particle physics. In the following, we highlight the main aspects that are relevant for our analysis.

In General Relativity, black hole superradiance is permitted in the case of Kerr black holes by the presence of the event horizon and the ergoregion [2–7]. The former is, for all intents and purposes, a one-way viscous membrane from which nothing, at least at the classical level, can escape. In other words, the presence of an event horizon makes black holes perfect absorbers. The latter is a region surrounding the event horizon where everything – literally, including light – is forced to co-rotate with the black hole. The presence of both the event horizon and the ergoregion creates the ideal conditions to make the Penrose process – that is the extraction of energy from a rotating black hole – possible [8]. Black hole superradiance can be thought of as the wave analogue of the Penrose process.

Superradiance has remarkable consequences in the presence of a confining mechanism, for instance provided by the presence of a perfectly reflecting mirror surrounding the black hole. In this case the amplified pulse bounces back and forth, exponentially increasing its amplitude, and eventually leading to an instability. This situation is naturally realized when the Kerr black hole is coupled to a massive boson since low-frequency radiation is confined due to a Yukawa-like suppression.

Let us make these points more quantitative following the same line of reasoning presented in [1, 7]. We consider a massive wave-packet in the gravitational field of a black hole. The situation is remarkably similar to that of an electron in the Coulomb potential of a hydrogen atom, and the problem – after introducing the tortoise coordinate r^* , with $r^* \rightarrow -\infty$ as r approaches the black hole horizon r_+ – reduces to the solution of a Schrödinger-like one-dimensional equation $d^2\Psi/dr^{*2} + V_{\text{eff}}(r)\Psi = 0$ describing the radial motion under the influence of an effective potential. For a Schwarzschild black hole of mass M the effective potential takes the form

$$V_{\text{eff}}^{\text{Schw}}(r) = \omega^2 - \left(1 - \frac{2G_N M}{r}\right) \left[\frac{2G_N M}{r^3} + \frac{l(l+1)}{r^2} + \mu^2\right], \quad (1)$$

where $G_N = (1/M_{\text{Pl}})^2$ is the Newton’s constant (with $M_{\text{Pl}} \simeq 1.22 \times 10^{19}$ GeV the Planck mass), ω is the frequency of the wave-packet, μ the scalar field mass, and l the azimuthal quantum number. The structure of eq. (1) remarks the analogy with the hydrogen atom mentioned before with a gravitational potential – instead of the usual Coulomb contribution – besides the centrifugal term. Asymptotically, considering both the horizon at $r \rightarrow r_+$ (equivalently, $r^* \rightarrow -\infty$) and spatially infinity at $r \rightarrow \infty$, the most general solution is

$$\Psi \sim \begin{cases} \mathcal{T}e^{-ik_+r^*} + \mathcal{O}e^{ik_+r^*} & r \rightarrow r_+, \\ \mathcal{R}e^{ik_\infty r^*} + \mathcal{I}e^{-ik_\infty r^*} & r \rightarrow \infty, \end{cases} \quad (2)$$

with $k_+^2 \equiv V_{\text{eff}}(r \rightarrow r_+)$, $k_\infty^2 \equiv V_{\text{eff}}(r \rightarrow \infty)$, and generic transmitted (\mathcal{T}), reflected (\mathcal{R}), incident (\mathcal{I}), and outgoing (\mathcal{O}) flux. In the following simplified discussion we assume the potential to be real even if this is not true in general because ω is a complex number. Since under this assumption the Schrödinger equation is real, the complex conjugate of any solution is also a solution. We can, therefore, impose the Wronskian equality $\mathcal{W}(\Psi, \Psi^*)|_{r \rightarrow r_+} = \mathcal{W}(\Psi, \Psi^*)|_{r \rightarrow \infty}$, with $\mathcal{W}(\Psi, \Psi^*) \equiv \Psi(\Psi^*)' - \Psi^*(\Psi)'$, and we find the unitarity condition [1]

$$|\mathcal{R}|^2 = |\mathcal{I}|^2 - \frac{k_+}{k_\infty} (|\mathcal{T}|^2 - |\mathcal{O}|^2) . \quad (3)$$

Notice that for a black hole at the horizon the outgoing flux at the horizon is zero, $\mathcal{O} = 0$, at least at the classical level. The wave is superradiant amplified, i.e. $|\mathcal{R}|^2 > |\mathcal{I}|^2$, if $k_+/k_\infty < 0$. For the Schwarzschild black hole in eq. (1) one immediately finds that $k_+/k_\infty|_{\text{Schw}} = \omega/\sqrt{\omega^2 - \mu^2}$, and the superradiant condition never happens. On the contrary, since $\mathcal{O} = 0$, we find $|\mathcal{R}|^2 < |\mathcal{I}|^2$ that is the typical case of an absorber material. Let us now move to the case of a Kerr black hole with mass M and angular momentum $J = aM$. The effective potential is more complicated (see eqs. (11, 12) below) but it is straightforward to find

$$\frac{k_+}{k_\infty} \Big|_{\text{Kerr}} = \left(\omega - \frac{am}{2G_N M r_+} \right) / \sqrt{\omega^2 - \mu^2} . \quad (4)$$

The superradiant condition is verified if $\omega < am/2G_N M r_+$, where $-l \leq m \leq l$ is the magnetic quantum number, and the reflected wave is superradiant amplified.

This simple example makes clear the general features of black hole superradiance outlined at the beginning of the section. First of all, the importance of the horizon. In the absence of an horizon – consider for instance a generic star – it is necessary to impose a regularity condition at the center. As a consequence of $d\Psi/dr|_{r \rightarrow 0} = 0$, the Wronskian at the center vanishes. The Wronskian at infinity gives $\mathcal{W}(\Psi, \Psi^*)|_{r \rightarrow \infty} = -2ik_\infty(|\mathcal{R}|^2 - |\mathcal{I}|^2) = 0$, and there is no superradiance since $|\mathcal{R}|^2 = |\mathcal{I}|^2$. More generally, this is the typical condition that occurs in the absence of a dissipative mechanism because in this case conservation of energy implies that the outgoing flux equals the transmitted one, $|\mathcal{T}|^2 = |\mathcal{O}|^2$, and the condition $|\mathcal{R}|^2 = |\mathcal{I}|^2$ follows from eq. (3).¹ Second, we see that the black hole spin $a \neq 0$ is crucial to fulfill the superradiant condition, and rotational energy powers the growth of the reflected wave in eq. (3). The extraction is made possible because the rotational energy of a Kerr black hole is not located inside the event horizon but in the ergoregion. This is the crucial difference compared to the Schwarzschild case, in which there is no energy available outside the event horizon. Finally, the presence of a mass term μ naturally provides a confining mechanism for the low-frequency reflected waves since if $\omega < \mu$ from $e^{ik_\infty r}$ and $k_\infty = \sqrt{\omega^2 - \mu^2}$ one gets a Yukawa-like suppression.

The striking conclusion that follows from this discussion is that, under the specific conditions that trigger a superradiant instability, in the presence of a massive scalar field it should

¹In the absence of an horizon, superradiance is possible only in the presence of an alternative dissipation mechanism. See [9] for an interesting recent example in the context of conducting rotating stars.

not be possible to observe fast-spinning black holes simply because the black hole must spin down as a consequence of energy extraction.² Black hole spin-measurements [13, 14] are therefore a valid experimental observable to constraint or discover new massive scalar particles [15]. As a rule of thumb, superradiance is relevant if the Compton wavelength of the massive particle $\lambda_{\text{Compton}} = 1/\mu$ is of the same order compared with the black hole radius $R \approx 2G_N M$

$$M \approx 6.7 \left(\frac{10^{-12} \text{ eV}}{\mu} \right) M_{\odot} . \quad (5)$$

Supermassive black hole with $M \sim 10^6 M_{\odot}$ corresponds to ultra-light scalar with $\mu \sim 10^{-18} \text{ eV}$ while stellar-mass black holes are relevant if $\mu \sim 10^{-12} \text{ eV}$. From a particle physics perspective, such light scalars are natural if protected by some underlying symmetry that makes the presence of a tiny mass term technically natural, and the most convincing case is that of a pseudo-Nambu-Goldstone boson, a light scalar field arising from the spontaneous breaking of a global symmetry. The QCD axion and, more generally, axion-like particles (ALPs) are typical examples. The former is theoretically motivated by the solution of the strong CP problem, the latter are ubiquitous in the low-energy limit of string constructions (the “axiverse” [16]). Black hole superradiance is, therefore, an extremely interesting discovery tool for this class of new physics particles.

However, the story told so far only relies on gravitational interactions. In other words, any boson with mass μ , irrespective of its particle physics origin, will display the same physics as far as the aforementioned picture of superradiance is concerned.

The goal of this paper is to present and discuss an observable consequence of black hole superradiance that is intimately connected to the axionic nature of the scalar cloud. To this end, we shall exploit the axion effective coupling to photons which is defined by the Lagrangian density

$$\mathcal{L}_{a\gamma\gamma} = \frac{g_{a\gamma\gamma}}{4} \Phi F_{\mu\nu} \tilde{F}^{\mu\nu} = -g_{a\gamma\gamma} \Phi \vec{E} \cdot \vec{B} . \quad (6)$$

In the case of the QCD axion this coupling – inherited from the mixing with light mesons (π_0 , η , η' , *et cetera*) as well as by the triangle anomaly of the Peccei-Quinn fermions – is in general non vanishing and it motivates a rich search strategy based on axion-photon conversion in external magnetic fields [17].

Our idea is very simple, and can be illustrated as follows. Consider an electromagnetic wave in the vacuum, defined by the wave vector $\hat{k} = \vec{k}/|\vec{k}|$ determining the direction of propagation, the angular frequency ω , and two basis polarization vectors $\hat{e}_{i=1,2}$, both being perpendicular to \hat{k} . Under parity, we have the transformation property $(\hat{k}, \hat{e}_1, \hat{e}_2) \xrightarrow{P} (\hat{k}, \hat{e}_1, -\hat{e}_2)$. The situation is illustrated in two steps in fig. 1. The wave vector \hat{k} flips sign as a consequence of the Fourier space identification $\vec{\nabla} \rightarrow i\vec{k}$. The two polarization vectors also flip sign. This is evident in the Coulomb gauge, in which $\vec{E} = i\omega\vec{A}$. The vector potential \vec{A} inherits the parity transformation property of the electric field, $\vec{E} \xrightarrow{P} -\vec{E}$. The Coulomb gauge is very useful because it exhibits the physical degrees of freedom: the 3 components of \vec{A} satisfy the

²Superradiance is also possible for a massive spin-1 [10, 11] and spin-2 field [12].

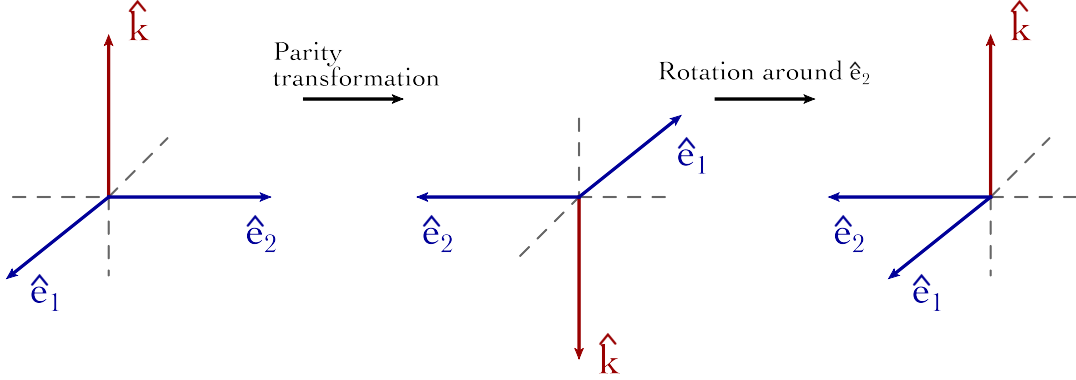


Figure 1: *Parity transformation for the triad $(\hat{k}, \hat{e}_1, \hat{e}_2)$. Under a genuine parity transformation $(\hat{k}, \hat{e}_1, \hat{e}_2) \xrightarrow{P} (-\hat{k}, -\hat{e}_1, -\hat{e}_2)$ (central panel). A further π rotation around the \hat{e}_2 axis (right panel), made possible by isotropy of space, brings the versors to the final configuration $(\hat{k}, \hat{e}_1, -\hat{e}_2)$.*

constraint $\vec{\nabla} \cdot \vec{A} = 0$, leaving behind the 2 degrees of freedom that can be identified with the polarization states of the photon. This means that one can write (for some numbers $a_{i=1,2}$ left unspecified) $\vec{A} = \sum_{i=1,2} a_i \hat{e}_i$, and the parity transformation of $\hat{e}_{i=1,2}$ follows from $\vec{A} \xrightarrow{P} -\vec{A}$. Finally, because of isotropy of space, only the relative orientation between vectors really matters. We can therefore apply a π rotation around the \hat{e}_2 axis in order to get the final parity transformation quoted above, $(\hat{k}, \hat{e}_1, \hat{e}_2) \xrightarrow{P} (\hat{k}, \hat{e}_1, -\hat{e}_2)$. This specific choice suggests to use left- and right-handed circular polarization vectors defined by $\hat{e}_{L,R} \equiv (\hat{e}_1 \mp i\hat{e}_2)/\sqrt{2}$ since under parity $\hat{e}_{L,R} \xrightarrow{P} \hat{e}_{R,L}$. In the absence of parity violation, there should be no difference in the physical properties of a right- and a left-handed circularly polarized electromagnetic wave. This discussion is of course a trivial consequence of parity invariance of electromagnetism.

The photon coupling in eq. (6) does not respect parity, since $\vec{E} \xrightarrow{P} -\vec{E}$ and $\vec{B} \xrightarrow{P} \vec{B}$. This implies that the left and right components of an electromagnetic wave traveling through an axion background should experience different physical effects. This is precisely what we shall explore in this paper considering the axion cloud surrounding a Kerr black hole as an optically active medium.

This paper is structured as follows. In section 2 we discuss general aspects of black hole superradiance with a particular emphasis on the conditions that allow for an analytical approach. In section 3 we compute the polarization-dependent bending that a ray of light experiences by traveling through an axion cloud, and in section 4 we discuss the phenomenological relevance of our result. Finally, we conclude in section 5. Further technical details are provided in the appendices.

2 Axion clouds around rotating black holes

The massive Klein-Gordon equation

$$\square\Phi = \mu^2\Phi \quad (7)$$

in a Kerr background

$$ds_{\text{Kerr}}^2 = -\left(1 - \frac{2Mr}{\Sigma}\right) dt^2 + \frac{\Sigma}{\Delta} dr^2 - \frac{4raM}{\Sigma} s_\theta^2 d\phi dt + \Sigma d\theta^2 + \left[(r^2 + a^2)s_\theta^2 + \frac{2rMa^2}{\Sigma} s_\theta^4\right] d\phi^2, \quad (8)$$

where $\Sigma = r^2 + a^2 c_\theta^2$, $\Delta = (r - r_+)(r - r_-)$, $r_\pm = M(1 \pm \sqrt{1 - \tilde{a}^2})$, $a = J/M$, $\tilde{a} = a/M$, admits the existence of quasi-bound states, as we shall briefly review in the following.

We use the short-hand notation $s_\theta \equiv \sin\theta$, $c_\theta \equiv \cos\theta$, and (t, r, θ, ϕ) are the usual Boyer-Lindquist coordinates. We work in natural units in which Planck's constant \hbar , the speed of light c , and Newton's constant G_N are set to one. Occasionally, we will reintroduce G_N to make some equations more transparent.

The massive Klein-Gordon equation in the Kerr background allows separation of variables³ with the following simple ansatz for the scalar field [7]

$$\Phi(t, r, \theta, \phi) = \sum_{l,m} e^{im\phi} S_{lm}(\theta) e^{-i\omega t} R_{nl}(r). \quad (9)$$

The angular equation defines the spheroidal harmonics $S_{lm}(\theta)$ [21]. The angular eigenvalues λ_{lm} are approximated by

$$\lambda_{lm} \simeq l(l+1) + \frac{2c^2 [m^2 - l(l+1) + 1/2]}{(2l-1)(2l+3)}, \quad (10)$$

where the so-called degree of spheroidicity c^2 is defined by $c^2 \equiv a^2(\omega^2 - \mu^2)$. The radial part, on the contrary, reduces to a Schrödinger-like problem. Defining the Regge-Wheeler tortoise coordinate $dr^* = [(r^2 + a^2)/\Delta]dr$, and rescaling the radial function according to $u_{nl}(r^*) = (r^2 + a^2)^{1/2} R_{nl}(r)$, the radial equation reads

$$\frac{d^2 u}{dr^{*2}} + [\omega^2 - V(\omega)] u = 0, \quad (11)$$

where the potential is

$$V = \frac{\Delta\mu^2}{r^2 + a^2} + \frac{4Mram\omega - a^2m^2 + \Delta[\lambda_{lm} + (\omega^2 - \mu^2)a^2]}{(r^2 + a^2)^2} + \frac{\Delta(3r^2 - 4Mr + a^2)}{(a^2 + r^2)^3} - \frac{3r^2\Delta^2}{(r^2 + a^2)^4}. \quad (12)$$

The relation between the tortoise coordinate r^* and the ordinary radial coordinate r is

$$r^* = r + \frac{2Mr_+}{(r_+ - r_-)} \ln\left(\frac{r}{r_+} - 1\right) - \frac{2Mr_-}{(r_+ - r_-)} \ln\left(\frac{r}{r_-} - 1\right). \quad (13)$$

³This property follows from the fact that the Kerr metric admits – among its mysterious “miracles” [18] – the existence of a Killing-Yano tensor [19, 20].

The radial equation must be solved with the following boundary conditions

$$R_{r^* \rightarrow -\infty} \sim e^{-ik_+ r^*}, \quad R_{r^* \rightarrow \infty} \sim \frac{1}{r} e^{i(\omega^2 - \mu^2)^{1/2} r^*}, \quad (14)$$

with $k_+ \equiv \omega - m\Omega_H$, being $\Omega_H \equiv a/2Mr_+$ the angular velocity of the Kerr black hole. Notice that we have purely ingoing waves at the horizon ($r^* = -\infty$ in tortoise coordinate); towards spatial infinity, on the contrary, the solution tends to zero since we are interested in bound states.

The manipulations above reduced the problem to the motion of a particle subject to the one-dimensional effective potential in eq. (12). We show the effective potential in the left

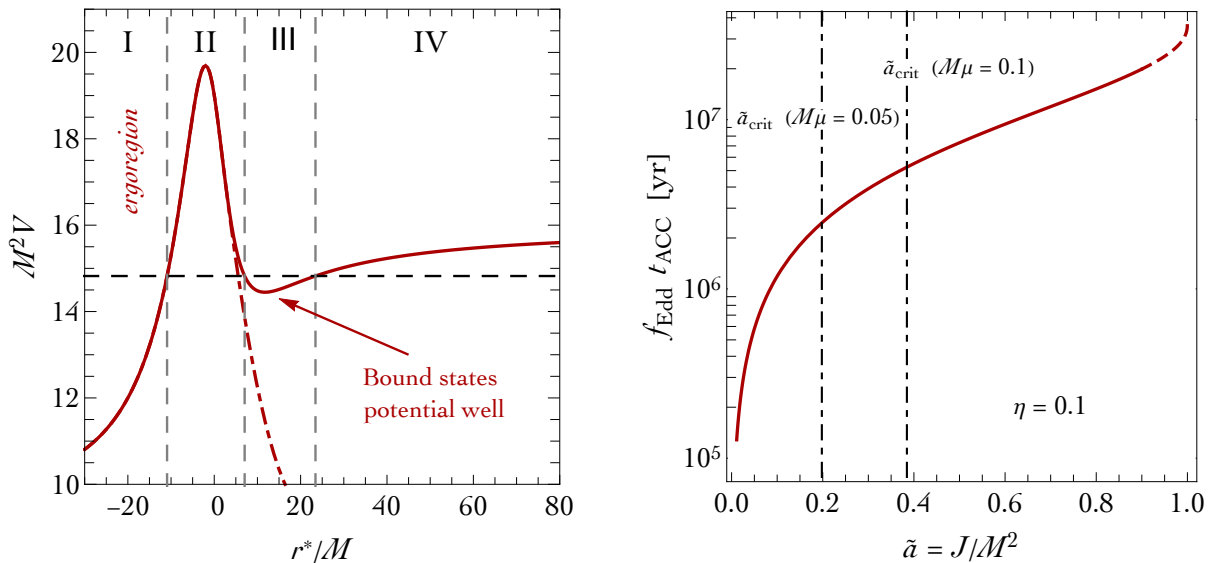


Figure 2: *Left panel.* Effective potential in eq. (12) as a function of the tortoise coordinate r^* . *Right panel.* Evolution of the black hole angular momentum due to accretion starting from the Schwarzschild limit. Vertical lines mark two critical conditions in eq. (22) for $m = 1$ and different values of $M\mu$. The solid red line becomes dashed where the inclusion of radiation is important.

panel of fig. 2. The presence of the mass term in the Klein-Gordon equation generates a potential well in region III, allowing for the formation of bound states. Notice that in the massless limit, the potential well cannot be formed (dot-dashed red line in the left panel of fig. 2). Gravitational and centrifugal effects create a potential barrier in region II, and the particle bounded in region III can tunnel in the black hole ergoregion, region I. If the phase velocity of the purely ingoing wave at the horizon is negative – that is if $\omega_R < m\Omega_H$ from the boundary condition in eq. (14), with $\omega_R \equiv \text{Re}(\omega)$ – the transmitted wave will carry negative energy into the black hole, and the reflected wave will return to infinity with greater amplitude and energy than the incident wave: The superradiance mechanism is triggered.

The growth of superradiant instability depends on the dimensionless product $M\mu$. This product represents the ratio between the horizon size of the black hole and the Compton

wavelength λ_{Compton} of the scalar field

$$M\mu \equiv \frac{G_N M \mu}{\hbar c} \sim \frac{r_+}{\lambda_{\text{Compton}}} . \quad (15)$$

Two limits are commonly used, $M\mu \ll 1$ and $M\mu \gg 1$. The crucial difference is the growth rate of bound states. Parametrically, we have the following order-of-magnitude estimates [6, 7, 15]

$$\tau \underset{M\mu \ll 1}{\approx} \frac{M}{(M\mu)^9} , \quad \tau \underset{M\mu \gg 1}{\approx} 10^7 e^{3.7(M\mu)} M . \quad (16)$$

In the limit $M\mu \ll 1$ the growth of superradiant instability can be as short as 10^2 s for stellar black holes

$$\tau \sim 10^2 \left(\frac{M}{10 M_\odot} \right) \left(\frac{0.2}{M\mu} \right)^9 \text{ s} , \quad (17)$$

while in the opposite limit the presence of the e -folding makes the instability insignificant for astrophysical black holes.

In the following we assume the small $M\mu$ limit, with

$$M\mu = 7.5 \times 10^{-2} \times \left(\frac{M}{10 M_\odot} \right) \times \left(\frac{\mu}{10^{-12} \text{ eV}} \right) . \quad (18)$$

The small $M\mu$ limit allows for a simple analytical understanding of superradiance.

In the small $M\mu$ limit, the eigenvalue problem for the radial equation admits an hydrogenic-like solution $\omega \equiv \omega_R + i\omega_I$ [7]

$$\omega_R \simeq \mu - \frac{\mu}{2} \left(\frac{M\mu}{l+n+1} \right)^2 , \quad (19)$$

$$\omega_I \simeq \mathcal{F}_{nl} \frac{(M\mu)^{4l+5}}{M} \left(\frac{am}{M} - 2\mu r_+ \right) \prod_{j=1}^l \left[j^2 \left(1 - \frac{a^2}{M^2} \right) + \left(\frac{am}{M} - 2\mu r_+ \right)^2 \right] , \quad (20)$$

with

$$\mathcal{F}_{nl} \equiv \frac{2^{4l+2} (2l+1+n)!}{(l+n+1)^{2l+4} n!} \left[\frac{l!}{(2l)!(2l+1)!} \right]^2 . \quad (21)$$

The eigenfrequencies are, in general, complex, and the superradiance condition reads

$$a_{\text{crit}} \sim \frac{2\mu r_+ M}{m} . \quad (22)$$

When $a > a_{\text{crit}}$, the imaginary part of ω becomes positive: The corresponding modes increase in time, signaling an instability of the Kerr black hole in the presence of the massive scalar field.

In the small $M\mu$ limit, the radial eigenfunction reads [7, 22] (see also appendix A)

$$R_{nl}(r) = A_{nl} g(\tilde{r}) , \quad g(\tilde{r}) \equiv \tilde{r}^l e^{-\tilde{r}/2} L_n^{2l+1}(\tilde{r}) , \quad \tilde{r} \equiv \frac{2r M \mu^2}{l+n+1} , \quad (23)$$

with $L_n^{2l+1}(\tilde{r})$ the Laguerre polynomials. In analogy with the hydrogen atom, the combination $\nu \equiv l + n + 1$ defines the principal quantum number.

It is important to notice that the size of the cloud can be estimated as [15]

$$r_{\text{cloud}} \sim \frac{(l+n+1)^2 M}{(M\mu)^2} \sim (l+n+1)^2 \times 1.5 \times 10^3 \left(\frac{M}{M_\odot}\right) \left(\frac{0.1}{M\mu}\right)^2 \text{ km} . \quad (24)$$

It implies that the cloud extends way beyond the horizon, where rotation effects can be neglected. In this limit the spheroidal harmonics $S_{lm}(\theta)$ reduce to the flat space spherical harmonics.

As clear from the previous discussion, superradiance is a dynamical process. It is therefore crucial to specify what are the assumption underlying our analysis. The physical setup we have in mind is the following.

1. Let us start considering a rotating black hole. In order to trigger the superradiant instability, the black hole must spin above the critical value in eq. (22). We can not take this condition for granted, given in particular the lack of unambiguous experimental informations about black hole spins at birth. However, it is not difficult to imagine physical processes by means of which a black hole, even starting from a slowly-rotating configuration, increases its mass and spin, eventually fulfilling the superradiant condition. The simplest possibility is provided by accretion. Astrophysical black holes are generally surrounded by an accretion disk of matter in the form of gas and plasma, and the inner edge of this disk is located in the equatorial plane at the position of the innermost stable circular orbit, r_{ISCO} . From r_{ISCO} , because of the pull of gravitational attraction, particles are sucked into the black hole increasing its mass and angular momentum. We can, therefore, ask the following crude question. What is the typical time scale needed to increase, via accretion, the spin of a non-rotating Schwarzschild black hole with initial mass M_{in} to maximally-rotating values? The accretion of a certain amount of rest mass ΔM_0 results into a change of the black hole mass M and spin J given by $\Delta J = l(z, M)\Delta M_0$ and $\Delta M = e(z)\Delta M_0$ [23, 24],⁴ where $z \equiv r_{\text{ISCO}}/M$, $e(z)$ is the energy per unit rest mass and $l(z, M)$ is the angular momentum per unit rest mass for a particle in the vicinity of the black hole. The explicit expressions can be found in [25]. A simple algebraic manipulation leads to a first-order differential equation that can be solved with the Schwarzschild initial condition $z_{\text{in}} = 6$. All in all, we find [25]

$$\tilde{a}(M) = \left(\frac{2}{3}\right)^{1/2} \frac{M_{\text{in}}}{M} \left\{ 4 - \left[18 \left(\frac{M_{\text{in}}}{M}\right)^2 - 2 \right]^{1/2} \right\} . \quad (25)$$

To fix ideas, eq. (25) implies, for instance, that $\tilde{a} = 0.6$ when $M/M_{\text{in}} \simeq 1.25$. Having set the relation between mass and spin, we now need an expression for the mass accretion

⁴In our simplified discussion we do not include the contribution from radiation, i.e. the torque produced by photons emitted from the surface of the accretion disk. As shown in [24], radiation limits the maximum spin to $\tilde{a} \lesssim 0.998$. The inclusion of radiation is, therefore, important to prevent violation of the cosmic censorship hypothesis but it is not crucial for our argument.

rate. Following [26], we assume the mass accretion rate to be proportional to the Eddington rate $\dot{M} = f_{\text{Edd}}\dot{M}_{\text{Edd}} = f_{\text{Edd}}(4\pi G_N M m_p / \eta \sigma_T)$, where η is the efficiency, m_p the proton mass and $\sigma_T \approx 1.7 \times 10^3 \text{ GeV}^{-2}$ the Thompson cross-section. We take $\eta = 0.1$. The reader should keep in mind that this is a very conservative estimate. It is indeed possible to imagine values of \dot{M} much greater than the ones inferred by using the Eddington formula by making the accretion disk physically thick, and with low density. By integrating the mass accretion formula we find the following expression for the accretion time t_{ACC}

$$\ln \frac{M}{M_{\text{in}}} = f_{\text{Edd}} \left(\frac{4\pi G_N m_p}{\eta \sigma_T} \right) t_{\text{ACC}} , \quad (26)$$

where in the left-hand side the ratio M/M_{in} can be obtained by inverting eq. (25). In the right panel of fig. 2 we show the product $f_{\text{Edd}}t_{\text{ACC}}$ in years (yr) as a function of the black hole spin. As mentioned above, the computation of t_{ACC} is subject to some astrophysical uncertainty, and the only intent of our plot is to show that, even starting from the borderline case of a Schwarzschild black hole, it is possible to reach critical values of spin in a finite amount of time. We refer the reader to [26] for a more detailed numerical study about the interplay between accretion and superradiance, and for the rest of the paper we will assume that the scalar cloud is not directly coupled to the disk.

2. When the condition $a > a_{\text{crit}}$ is satisfied, the black hole rapidly loses its spin favoring the growth of the axion cloud. The cloud sprouts up from an initial seed that can be simply provided by a quantum fluctuation of the vacuum, as suggested in [27]. En route, we also note that Kerr black hole itself may naturally provide a source term for the axion field. This is because the Kerr metric in eq. (8) has non-vanishing Hirzebruch signature density $R\tilde{R}$ [28]. By explicit computation, we find

$$\frac{1}{2}R\tilde{R} \equiv \frac{1}{2}\epsilon^{\alpha\beta\mu\nu} R_{\rho\lambda\alpha\beta} R_{\mu\nu}{}^{\rho\lambda} = \frac{\epsilon^{\alpha\beta\mu\nu}}{2\sqrt{-g}} R_{\rho\lambda\alpha\beta} R_{\mu\nu}{}^{\rho\lambda} = \frac{288 \tilde{a} M^3 \cos \theta}{r^7} + \mathcal{O}(\tilde{a}^2) . \quad (27)$$

$R\tilde{R}$ is proportional to the spin, and vanishes for a Schwarzschild black hole. If the electromagnetic field is quantized in a gravitational background with such property, the pseudo-scalar combination $F_{\mu\nu}\tilde{F}^{\mu\nu}$ acquires a non-vanishing expectation value $F_{\mu\nu}\tilde{F}^{\mu\nu} = R\tilde{R}/48\pi^2$ [29] which, in turn, acts like a background source term for the axion field via the usual electromagnetic coupling. After this digression, let us now go back to the growth of the axion cloud. In the left panel of fig. 3 we show the superradiance rates in eq. (20) – in units of M^{-1} – for different levels. In the small $M\mu$ limit the fastest superradiant level is the $2p$ level with $n = 0$ and $l = m = 1$. The black hole loses its spin by populating the $2p$ shell while all the remaining ones can be neglected. As already noticed in eq. (16), this process can be as short as 10^2 s for stellar black holes.

3. The spin-down of the black hole continues until it reaches the threshold value given by eq. (22) with $m = 1$. The imaginary part in eq. (20) vanishes, and the spin-down process

terminates. The black hole remains in this state for a period of time that can be very long. Indeed, the next $3d$ level of the axion cloud does not start being populated until a large enough number of axions dissipate from the $2p$ level. In this respect, annihilation into gravitons and annihilation into unbounded axions due to self-interactions are the most efficient processes [15]. As soon as the the cloud mass drops below a critical value, superradiance becomes operative again, and the black hole rapidly travels to the next level. As discussed in [15], the time required for an axion cloud in the $2p$ level to dissipate such that the next superradiant level can start being populated can be extremely long – specially in the small $M\mu$ limit. To give a concrete idea, the annihilation time – considering the $2p \rightarrow 3d$ transition – can be computed as follows. We start writing in full generality the time evolution of the axion population in the $2p$ level due to axion annihilation into gravitons as $dN/dt = -\Gamma_{\text{ann}}N^2$. The annihilation rate Γ_{ann} is given by

$$\Gamma_{\text{ann}} = \frac{1}{2\omega N^2} \int d\Omega \frac{dP}{d\Omega} , \quad (28)$$

where N is the number of axions and $\int d\Omega dP/d\Omega \equiv dE_{\text{GW}}/dt$ is the energy per unit of time emitted into gravitational radiation. When the superradiance condition is satisfied the imaginary part of ω vanishes, and in the small $M\mu$ limit we have $\omega_{\text{R}} \approx \mu$. The computation of dE_{GW}/dt cannot be performed in flat space because the leading term in the small $M\mu$ expansion accidentally cancels. We therefore use the corresponding expression derived in the Schwarzschild background metric [26]

$$\frac{dE_{\text{GW}}}{dt} = \frac{484 + 9\pi^2}{23040} \left(\frac{M_S^2}{M^2} \right) (M\mu)^{14} , \quad (29)$$

where M_S is the mass of the axion cloud. Furthermore, since axions are non-relativistic, we can write $M_S = N\mu$. Eq. (29) is in good agreement with the computation recently performed in [30, 31] using the Teukolsky formalism in the fully relativistic regime. We can now integrate $dN/dt = -\Gamma_{\text{ann}}N^2$, and find

$$N(t) = \frac{N(0)}{1 + \Gamma_{\text{ann}}N(0)t} \approx \frac{1}{\Gamma_{\text{ann}}t} . \quad (30)$$

In order to proceed further, we use the condition according to which the $3d$ level starts being populated when the number of axions in the $2p$ level drops below the value [15]

$$N \lesssim \frac{16\pi f_a^2 M^2}{(M\mu)^3} \left| \frac{\Gamma_{3d}}{\Gamma_{1s}} \right|^{1/2} . \quad (31)$$

The presence in eq. (31) of the damping rate related to the level $1s$ is due to the effect of axion non-linearities. These interactions are responsible for level mixing, and introduce a superposition of the $2p$ level with the non-superradiant $1s$ mode. In our example – remember that we are considering a black hole spin such that the superradiant condition in eq. (22) vanishes for the $2p$ level – the frequency of the $1s$ mode has a negative

imaginary part, and the level is damped. In the small $M\mu$ limit we compute the rate Γ_i using the imaginary frequencies in eq. (20). The condition derived in eq. (31) defines, plugged into eq. (29), the critical time scale

$$t_{\text{cr}} \simeq \left(\frac{720}{484 + 9\pi^2} \right) \frac{M}{\pi f_a^2 (M\mu)^{12}} \left| \frac{\Gamma_{1s}}{\Gamma_{3d}} \right|^{1/2}. \quad (32)$$

In fig. 3 we show the time in years to depopulate the level $2p$ for two representative value of black hole mass, $M = 50 M_\odot$ and $M = 10^6 M_\odot$, as a function of the axion coupling f_a and the parameter $M\mu$. From this estimate it is clear that in the small $M\mu$ limit the axion cloud can remain stuck for a very long time in the $2p$ level. It is therefore reasonable to focus on the values $l = m = 1, n = 0$. Motivated by these arguments, we adopt this assumption in the rest of the paper.

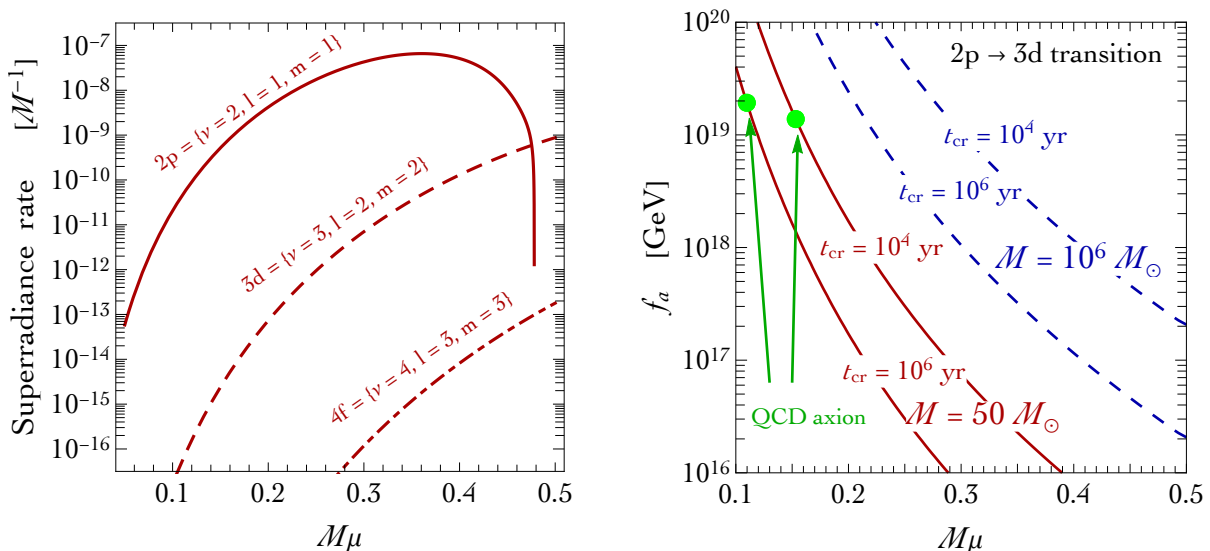


Figure 3: *Left panel.* Superradiant rates ω_I as a function of the dimensionless parameter $M\mu$ for different levels. *Right panel.* Time required for an axion cloud in the $2p$ level around a Kerr black hole with mass $M = 50 M_\odot$ (red solid lines) and $M = 10^6 M_\odot$ (blue dashed lines) to trigger a superradiant regime in the next $3d$ level as a function of the axion decay constant f_a and for different values of the parameter $M\mu$. For each $M\mu$, we compute the critical spin in eq. (22) and the rates Γ_{1s} and Γ_{3d} using the frequencies in eq. (20). The time scale of the transition is given by eq. (32). For each of the two analyzed black hole masses, the value of the parameter $M\mu$ fixes the axion mass μ . In the case of the QCD axion, the latter is related to a specific value of the axion decay constant f_a (see eq. (52) below). For a stellar black hole with mass $M = 50 M_\odot$, this correspondence is indicated in the plot with the green dots.

There are two scales in the problem, the oscillation time $\tau_S = 1/\omega_R$ and the instability

growth time scale $\tau \equiv 1/\omega_I$. In the small $M\mu$ limit we have

$$\omega_R = \mu - \frac{\mu}{2} \left(\frac{M\mu}{2} \right)^2 \approx \mu, \quad (33)$$

$$\omega_I = \frac{1}{48M} \left(\frac{a}{M} - 2\mu r_+ \right) (M\mu)^9 \approx \frac{(M\mu)^9}{M}. \quad (34)$$

As a consequence

$$\frac{\tau}{\tau_S} \approx \frac{1}{(M\mu)^8} \gg 1 \quad \Longrightarrow \quad \tau \gg \tau_S. \quad (35)$$

We can therefore assume a stationary cloud, and write

$$\Phi(t, r, \theta, \phi) = A_0 g(\tilde{r}) \cos(\phi - \omega_R t) \sin \theta, \quad A_0 \equiv A_{01}. \quad (36)$$

Notice that we focused on a real scalar cloud, since we have in mind the axions. The amplitude A_0 can be expressed in terms of the mass M_S of the scalar cloud [26]. In full generality, we write

$$M_S = \int \rho r^2 dr \sin \theta d\theta d\phi, \quad (37)$$

with $\rho = -T_0^0$. The energy density ρ can be directly computed from the definition of the stress-energy tensor

$$T^{\mu\nu}(\Phi) = (D^\mu \Phi)(D^\nu \Phi) - g^{\mu\nu} \left[\frac{g^{\rho\sigma}}{2} (D_\rho \Phi)(D_\sigma \Phi) + V(\Phi) \right], \quad (38)$$

where $V(\Phi) = \mu^2 \Phi^2/2$. Assuming flat space – see comment below eq. (24) – we find

$$\begin{aligned} \rho = & \frac{A_0^2}{2r^2} \left\{ \mu^4 M^2 r^2 g'(\tilde{r})^2 \sin^2 \theta \cos^2(\phi - \omega_R t) \right. \\ & \left. + g(\tilde{r})^2 \left[\cos^2(\phi - \omega_R t) (\cos^2 \theta + \mu^2 r^2 \sin^2 \theta) + \sin^2(\phi - \omega_R t) (1 + \omega_R^2 r^2 \sin^2 \theta) \right] \right\}. \end{aligned} \quad (39)$$

The integral in eq. (37) can be straightforwardly computed, and we find

$$M_S = \frac{2\pi A_0^2}{3M\mu^2} \left[2\mathcal{I}_0 + \mathcal{I}'_2 + \frac{2\mathcal{I}_2}{M^2\mu^2} \right], \quad \mathcal{I}_n = \int_0^\infty dx x^n g(x)^2, \quad \mathcal{I}'_n = \int_0^\infty dx x^n g'(x)^2. \quad (40)$$

In the small $M\mu$ limit we have

$$A_0^2 = \frac{3}{4\pi\mathcal{I}_2} \left(\frac{M_S}{M} \right) (M\mu)^4, \quad \text{with } \mathcal{I}_2 = 24. \quad (41)$$

The scalar cloud in eq. (36) becomes

$$\Phi = \sqrt{\frac{3}{4\pi\mathcal{I}_2}} \left(\frac{M_S}{M} \right) (M\mu)^2 g(\tilde{r}) \cos(\phi - \omega_R t) \sin \theta. \quad (42)$$

Considering for definiteness the value of the cloud at r_{cloud} in eq. (24), we have

$$r_{\text{cloud}} \sim \frac{4M}{(M\mu)^2}, \quad \tilde{r}_{\text{cloud}} \sim 4 \quad \Longrightarrow \quad g(\tilde{r}_{\text{cloud}}) \sim 0.5. \quad (43)$$

Furthermore, notice that the function $g(\tilde{r})$ has a maximum (for $l = 1$) at $\tilde{r}_{\max} = 2$.

Before proceeding, let us comment about possible limiting factors for the size of the cloud, in particular the so-called ‘‘bosonova’’ collapse [15]. The physics of the bosonova collapse can be summarized as follows. In the first stage, the energy of the cloud grows by superradiant instability. As the ratio M_S/M increases, the field amplitude in eq. (42) becomes larger – eventually saturating the condition $\Phi/f_a \sim 1$. At this point, the nonlinear self-interaction of the axion field becomes important, and causes a rapid collapse of the cloud. The analysis in [15] (see also [32] for a numerical analysis) implies the condition

$$\frac{M_S}{M} \lesssim \frac{2l^4 f_a^2}{(M\mu)^4 M_{\text{Pl}}^2}. \quad (44)$$

In the situation where $M\mu$ is small and f_a is large, the right-hand side of eq. (44) becomes large. In this case, the axion cloud spins down the black hole to reach the marginal superradiant condition, $\mu = m\tilde{a}/2r_+$, well before the nonlinear self-interaction becomes important. In this case, therefore, the main limiting factor is the initial rotation energy of the black hole.

Finally, we note that the typical axionic hair configurations generated by quantum effects [33–37] are usually suppressed, if compared with eq. (42), by the factor

$$\left(\frac{M_{\text{Pl}}}{M}\right)^2 \sim \frac{10^{-76}}{(M/M_\odot)^2}. \quad (45)$$

However, these quantum effects may act as a seed for the axion cloud (see discussion related to eq. (27)).

3 Polarization-dependent bending of light

The Maxwell field equations in the presence of a background axion field are

$$\vec{\nabla} \cdot \vec{E} = -g_{a\gamma\gamma} \vec{\nabla} \Phi \cdot \vec{B}, \quad (46)$$

$$\vec{\nabla} \times \vec{E} + \frac{\partial \vec{B}}{\partial t} = 0, \quad (47)$$

$$\vec{\nabla} \times \vec{B} - \frac{\partial \vec{E}}{\partial t} = g_{a\gamma\gamma} \left(-\vec{E} \times \vec{\nabla} \Phi - \vec{B} \frac{\partial \Phi}{\partial t} \right), \quad (48)$$

$$\vec{\nabla} \cdot \vec{B} = 0, \quad (49)$$

where $g_{a\gamma\gamma}$ is the effective coupling defined by the Lagrangian density

$$\mathcal{L}_{a\gamma\gamma} = \frac{g_{a\gamma\gamma}}{4} \Phi F_{\mu\nu} \tilde{F}^{\mu\nu} = -\frac{g_{a\gamma\gamma}}{2} (\partial_\mu \Phi) A_\nu \tilde{F}^{\mu\nu}, \quad (50)$$

with $\tilde{F}^{\mu\nu} = \epsilon^{\mu\nu\rho\sigma} F_{\rho\sigma}/2$. The effective coupling $g_{a\gamma\gamma}$ can be related to the axion decay constant f_a [38]

$$g_{a\gamma\gamma} = \frac{\alpha_{\text{em}}}{2\pi f_a} \left[\frac{E}{N} - \frac{2}{3} \left(\frac{4m_d + m_u}{m_d + m_u} \right) \right] = \frac{\alpha_{\text{em}}}{2\pi f_a} \left(\frac{E}{N} - 1.92 \right), \quad (51)$$

where E/N is the model-dependent ratio of the electromagnetic and color anomaly while the second term is a model-independent contribution coming from the minimal coupling to QCD at the non-perturbative level. The typical axion window is defined by the interval $0.07 \leq |E/N - 1.92| \leq 7$ [39]. Of particular interest are the reference values $E/N = 8/3$ (as in DFSZ models [40, 41] or KSVZ [42, 43] models with heavy fermions in complete $SU(5)$ representations) and $E/N = 0$ (as in KSVZ models with electrically neutral heavy fermions). Recently [44], the aforementioned axion window was redefined in light of precise phenomenological requirements – such as the absence of Landau poles up to the Planck scale or the need to avoid overclosure of the Universe – related to the representations of the new heavy quarks that are needed in KSVZ-type models to induce the anomalous coupling of the axion with ordinary quarks. As a result, the window $0.25 \leq |E/N - 1.92| \leq 12.25$ was singled out in the case of one single pair of new heavy fermions. Furthermore, with the inclusion of additional pairs of new heavy quarks values as large as $E/N = 170/3$ become accessible. Note that it is also possible to construct models with multiple scalars in which the value of $g_{a\gamma\gamma}$ in eq. (51) can be made arbitrarily large. We shall further explore this possibility in section 3.2.

For the QCD axion, the axion mass and decay constant are related by [38]

$$\frac{10^{16} \text{ GeV}}{f_a} = \frac{\mu}{5.7 \times 10^{-10} \text{ eV}}. \quad (52)$$

Only space-time gradients of the axion field configuration alter the Maxwell equations, since for a constant axion field $\Phi F_{\mu\nu} \tilde{F}^{\mu\nu}$ becomes a perfect derivative and does not affect the equation of motion. We assume that the length scale over which Φ changes appreciably is much larger than the wavelength λ of the electromagnetic wave. Within this approximation we can neglect in eqs. (46-49) terms containing second derivative (or first derivative squared) of Φ [45]. Let us briefly discuss the validity of this assumption. Considering the radial direction, the characteristic length scale of the cloud can be estimated using eq. (24). The condition on the wavelength λ reads

$$\lambda \ll r_{\text{cloud}} \sim 2.6 \times 10^6 \left(\frac{10 M_{\odot}}{M} \right) \left(\frac{10^{-12} \text{ eV}}{\mu} \right)^2 \text{ m}. \quad (53)$$

From eq. (42), the characteristic length scale of time variation is $\tau_S = 1/\omega_R$; since we are interested in the small $M\mu$ limit in which $\omega_R \simeq \mu$, we have the following condition on the wavelength λ

$$\lambda \ll \lambda_{\text{Compton}} \sim 2 \times 10^5 \left(\frac{10^{-12} \text{ eV}}{\mu} \right) \text{ m}. \quad (54)$$

Clearly, the conditions $\lambda \ll r_{\text{cloud}}, \lambda_{\text{Compton}}$ are verified for wavelength λ of astrophysical interest. The field equations take the form [45]

$$\square \left(\vec{E} - \frac{g_{a\gamma\gamma}}{2} \Phi \vec{B} \right) = -\frac{g_{a\gamma\gamma}}{2} \Phi \square \vec{B}, \quad (55)$$

$$\square \left(\vec{B} + \frac{g_{a\gamma\gamma}}{2} \Phi \vec{E} \right) = \frac{g_{a\gamma\gamma}}{2} \Phi \square \vec{E}, \quad (56)$$

and reduce to the usual electromagnetic wave equations in the limit $g_{a\gamma\gamma} \rightarrow 0$. Photon propagation is described by the following dispersion relation [46]

$$k^4 + g_{a\gamma\gamma}^2 (\partial_\mu \Phi)(\partial^\mu \Phi) k^2 = g_{a\gamma\gamma}^2 [k_\mu (\partial^\mu \Phi)]^2, \quad (57)$$

where $k^\alpha = (E_\gamma, \vec{k})$ is the four-momentum of the propagating photon. We give a derivation of eq. (57) in appendix B. At the first order, we have

$$E_\gamma^2 - |\vec{k}|^2 \approx \pm g_{a\gamma\gamma} \left[E_\gamma \frac{\partial \Phi}{\partial t} - \vec{k} \cdot \vec{\nabla} \Phi \right], \quad (58)$$

where the sign \pm corresponds to right- and left-handed circularly polarized waves. In eq. (58) we used a flat background metric. The gradient of the scalar field, in spherical coordinates, is

$$\vec{\nabla} \Phi = \left(\frac{\partial \Phi}{\partial r}, \frac{1}{r} \frac{\partial \Phi}{\partial \theta}, \frac{1}{r \sin \theta} \frac{\partial \Phi}{\partial \phi} \right) \xrightarrow{\theta=\pi/2} \left(\frac{\partial \Phi}{\partial r}, 0, \frac{1}{r} \frac{\partial \Phi}{\partial \phi} \right), \quad (59)$$

where in the last passage we restrict the analysis to the equatorial plane. Eq. (58) reads

$$\left(\frac{dr}{d\xi} \right)^2 = E_\gamma^2 - \frac{L^2}{r^2} \mp g_{a\gamma\gamma} \left\{ E_\gamma \frac{\partial \Phi}{\partial t} - \left[\left(\frac{dr}{d\xi} \right) \frac{\partial \Phi}{\partial r} + \frac{L}{r^2} \frac{\partial \Phi}{\partial \phi} \right] \right\}, \quad (60)$$

where ξ is the affine parameter while E_γ and L are, respectively, the conserved energy and angular momentum of the photon, with $k^r \equiv dr/d\xi$, $k^\theta \equiv d\theta/d\xi = 0$, $k^\phi \equiv d\phi/d\xi = L/r^2$. From eq. (42), we have

$$\frac{\partial \Phi}{\partial t} = \sqrt{\frac{3}{4\pi\mathcal{I}_2} \left(\frac{M_S}{M} \right)} (M\mu)^2 g(\tilde{r}) \omega_R \sin(\phi - \omega_R t), \quad (61)$$

$$\frac{\partial \Phi}{\partial r} = \sqrt{\frac{3}{4\pi\mathcal{I}_2} \left(\frac{M_S}{M} \right)} (M\mu)^2 g'(\tilde{r}) (M\mu)^2 \cos(\phi - \omega_R t), \quad (62)$$

$$\frac{1}{r} \frac{\partial \Phi}{\partial \phi} = -\frac{1}{r} \sqrt{\frac{3}{4\pi\mathcal{I}_2} \left(\frac{M_S}{M} \right)} (M\mu)^2 g(\tilde{r}) \sin(\phi - \omega_R t). \quad (63)$$

Notice that natural units can be recovered with the formal substitution $M \rightarrow G_N M$. Considering the radial distance at \tilde{r}_{\max} , we have

$$\frac{\partial \Phi}{\partial r}, \frac{1}{r} \frac{\partial \Phi}{\partial \phi} \sim (M\mu) \frac{\partial \Phi}{\partial t} \quad \xrightarrow{M\mu \ll 1} \quad \frac{\partial \Phi}{\partial t} \gg \frac{\partial \Phi}{\partial r}, \frac{1}{r} \frac{\partial \Phi}{\partial \phi}. \quad (64)$$

This relation simplifies the equation for the photon orbit in the presence of the axion background field. The differential equation for the photon orbit (see appendix C) is

$$\frac{d\phi}{dx} = -\frac{1}{x^2 \sqrt{\frac{1}{x_{\max}^2} - \frac{1}{x^2}}} \mp \frac{a(E_\gamma, x, \phi) - a(E_\gamma, x_{\max}, \frac{\pi}{2})}{2x^2 x_{\max}^2 \left(\frac{1}{x_{\max}^2} - \frac{1}{x^2} \right)^{3/2}}, \quad \text{with } a(E_\gamma, r, \phi) \equiv \frac{g_{a\gamma\gamma}}{E_\gamma} \frac{\partial \Phi}{\partial t} \Big|_{r, \phi}, \quad (65)$$

with dimensionless variable $x \equiv r/M$ (which of course corresponds to $x \equiv r/G_N M$ in natural units), and must be integrated between $x_0 = \infty$ and $x_{\max} = 2/(M\mu)^2$. The choice $x_0 = \infty$ practically means that we are considering a source and an observer at distance much larger than the impact parameter (see appendix C for a detailed discussion).

The outcome of this computation is the angular separation $|\Delta\phi_+ - \Delta\phi_-|$ between left- and right-handed circularly polarized waves that a ray of light experiences by traveling through the axion cloud.

In the following we shall solve this equation for the QCD axion and for a generic ALP. In section 4 we shall explain in more detail what is the phenomenological relevance of our computation.

3.1 The QCD axion

Stellar black hole superradiance in the presence of an ultra-light scalar field may produce in the next few years spectacular signatures – both direct and indirect – in gravitational wave detectors such as Advanced LIGO. Indirect signatures refer to the observation of gaps in the spin-mass distribution of final state black holes produced by binary black hole mergers. Direct signatures refer to monochromatic gravitational wave signals produced during the dissipation of the scalar condensate after the superradiant condition is saturated. In [27] it was shown that spin and mass measurements of stellar-size black holes exclude the QCD axion mass window $6 \times 10^{-13} \lesssim \mu [\text{eV}] \lesssim 2 \times 10^{-11}$, corresponding to $3 \times 10^{17} \lesssim f_a [\text{GeV}] \lesssim 10^{19}$. It is worth emphasizing that this bound is most likely only indicative since it is based on black hole spin measurements that are extracted indirectly from X-ray observations of accretion disks in X-ray binaries. We only have very few of such measurements at our disposal, and it is difficult to extract a bound with robust statistical confidence.

As far as direct signatures are concerned, a careful assess of the detection prospects in Advanced LIGO and LISA was recently proposed in [30, 31]. The outcome of the analysis is that, considering optimistic astrophysical models for black hole populations, the gravitational wave signal produced by superradiant clouds of scalar bosons with mass in the range

$$2 \times 10^{-13} \lesssim \mu [\text{eV}] \lesssim 10^{-12} , \quad (66)$$

is observable – i.e. it is characterized by a signal-to-noise ratio larger than the experimental threshold – by Advanced LIGO. For the QCD axion the mass range in eq. (66) corresponds to $5.7 \times 10^{18} \lesssim f_a [\text{GeV}] \lesssim 2.8 \times 10^{19}$. In the following, we shall adopt the mass interval in eq. (66) as benchmark for our analysis in the case of the QCD axion. However, before proceeding, an important comment is in order. For large values of f_a non-perturbative gravitational instantons become important, as discussed in [47]. If computed in the context of General Relativity, these effects generate a gravitational correction to the axion mass that increases with f_a and, if $f_a \gtrsim 10^{16}$ GeV, overcomes the QCD term in eq. (52). This effectively produces a lower limit on the QCD axion mass, $\mu \gtrsim 4.8 \times 10^{-10}$ eV [47]. From this perspective, the mass range in eq. (66) is theoretically disfavored. As discussed in [47] (see also [48] for the original

formulation of the argument), the computation of non-perturbative gravitational effects – and as a consequence the validity of the lower limit on μ – can be invalidated if the UV completion of General Relativity is weakly coupled since in this case we expect new degrees of freedom to become dynamical even below M_{Pl} . For this reason, it is important to keep investigating Planckian values of f_a since they may open an indirect window on quantum gravity effects.

The QCD axion with mass in the range given by eq. (66) falls into the so-called “anthropic” window. The Peccei-Quinn symmetry is broken before the end of inflation, and the possibility to reproduce the observed dark matter relic density $\Omega_{\text{DM}} h^2 \simeq 0.1$ relies on a fine-tuned choice of the initial misalignment angle θ_{in} . We find $1.19 \lesssim \theta_{\text{in}} \times 10^5 \text{ [rad]} \lesssim 3.98$ for the mass interval in eq. (66).

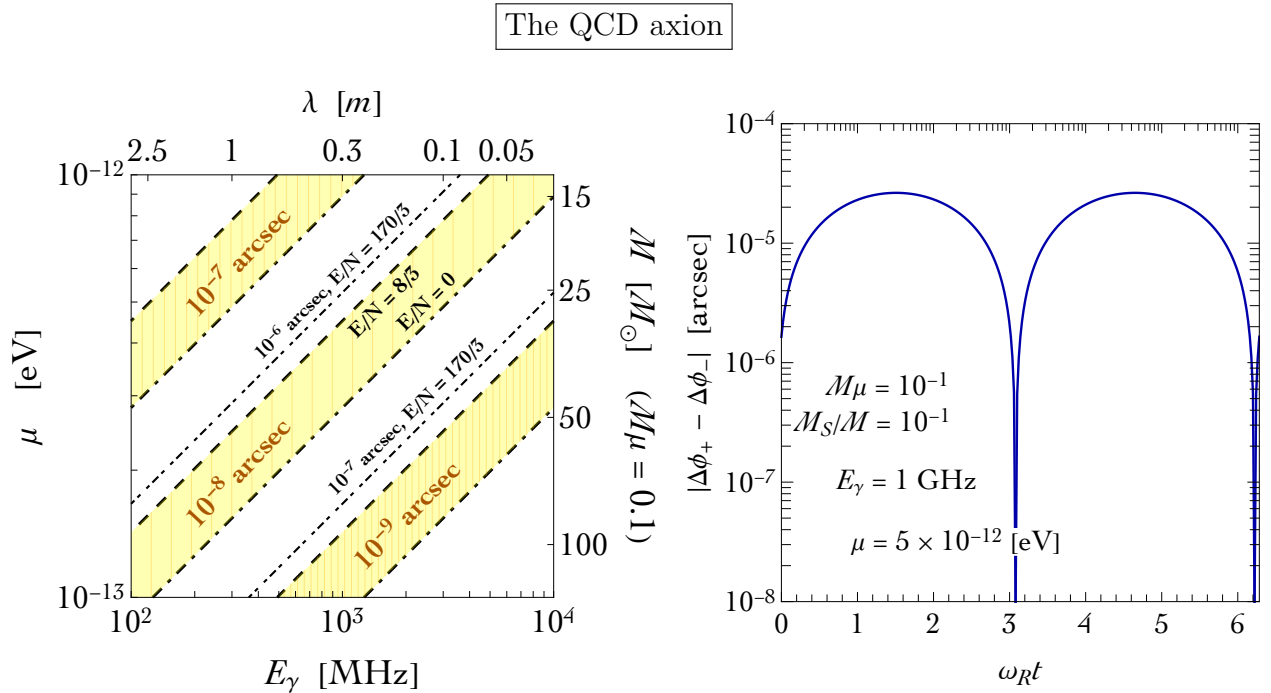


Figure 4: *Left panel.* Contours of constant angular splitting $|\Delta\phi_+ - \Delta\phi_-|$ (for fixed time t) as a function of the radio wave energy E_γ and the QCD axion mass μ . We fix $M\mu = M_S/M = 10^{-1}$, and we explore different possibilities for the electromagnetic-to-color anomaly ratio E/N in eq. (51). *Right panel.* Time-dependence of the angular splitting $|\Delta\phi_+ - \Delta\phi_-|$ for fixed QCD axion mass and radio wave energy. The period of the signal is set by the inverse of $\omega_R \approx \mu$, and we have $1/\mu \approx 0.66 \times 10^{-3} (10^{-12} \text{ eV}/\mu) \text{ s}$.

We show our result in fig. 4. We imagine a ray of light with energy E_γ traveling through the axion cloud, and in the left panel we plot (at fixed t) the angular splitting $|\Delta\phi_+ - \Delta\phi_-|$ as a function of E_γ and the axion mass μ . We fix $M\mu = M_S/M = 10^{-1}$, and we consider different values for the parameter E/N in eq. (51). Since $M\mu$ is fixed, at each value of μ corresponds a black hole mass M (respectively, left and right y axis). As expected, the QCD axion is relevant in connection with stellar-mass black holes. For typical values $0 < E/N < 8/3$, we obtain an angular splitting between left and right polarization of the order

$10^{-7} < |\Delta\phi_+ - \Delta\phi_-| [\text{arcsec}] < 10^{-9}$. As we shall discuss in section 4, these values are probably too small for a detection since, even taking an optimistic view, it is not possible at present to reach angular resolutions below $\delta\theta \approx 10^{-6}$ arcsec. For the QCD axion $|\Delta\phi_+ - \Delta\phi_-| \simeq 10^{-6}$ arcsec can be obtained in the analyzed parameter space for $E/N = 170/3$ (dot-dashed black lines in fig. 4).

In the right panel of fig. 4 we show the time-dependence of $|\Delta\phi_+ - \Delta\phi_-|$ due to the rotation of the cloud. We choose $\mu = 5 \times 10^{-12}$ eV and fixed energy $E_\gamma = 1$ GHz. The signal displays the expected periodicity set by $T = 2\pi/\omega_R \simeq 2\pi/\mu$.

As far as the QCD axion is concerned, the relevance of the polarization-dependent bending seems to be quite modest. The reason is that eq. (51) and eq. (52) imply a very strong relation between the mass of the QCD axion and its coupling to photons, and the range explored in eq. (66) corresponds to a coupling $g_{a\gamma\gamma}$ that is too weak. However, this is not a lapidary conclusion. The way-out is that the relation between the axion mass and the axion-photon coupling can not be considered a solid prediction of QCD, in clear contrast with the relation between axion mass and axion decay constant. The latter is dictated by the minimization of the effective potential generated by the explicit breaking of the continuous global shift symmetry of the axion due to QCD instanton effects, and thus tightly linked to the solution of the strong CP problem. The former has a degree of model-dependence – a fact already clear from the discussion about the possible values of E/N below eq. (51) – that can be exploited. It is possible, therefore, to construct simple models in which the axion-photon coupling can be arbitrarily large without altering eq. (52). In the next section, we shall illustrate one explicit realization of this idea.

3.2 The photo-philic QCD axion

The photo-philic (γ_\heartsuit hereafter) QCD axion [49] is a specific realization of the clockwork mechanism proposed in [50, 51]. In its original incarnation, the clockwork is a renormalizable theory that consists in a chain of $\mathcal{N} + 1$ complex scalar fields with a $U(1)^{\mathcal{N}+1}$ global symmetry spontaneously broken at the scale f . The $U(1)^{\mathcal{N}+1}$ global symmetry is also explicitly broken in such a way to preserve a single $U(1)$ symmetry whose Nambu–Goldstone boson – eventually identified with the QCD axion in [49] – lives in a compact field space with a dimension that is set by the effective decay constant $f_a = 3^{\mathcal{N}} f \gg f$. The key idea of [49] is the following. New vector-like fermions which are responsible for the generation of the color anomaly are coupled to the last site \mathcal{N} of the scalar chain. This guarantees the usual solution of the strong CP problem with the important difference that the scale $f_a = 3^{\mathcal{N}} f$ entering in eq. (52) can be parametrically much larger than the fundamental symmetry breaking scale f . This feature has very important phenomenological consequences because the model predicts the presence of additional pseudo-scalar particles which can be light and accessible at the LHC while keeping f_a above the astrophysical bounds (roughly $f_a \gtrsim 10^9$ GeV). In the usual realization of the QCD axion presented in section 3.1, the same vector-like fermions mediating the QCD anomaly also contribute to the axion-photon coupling. In the γ_\heartsuit QCD axion, on

the contrary, there are additional electromagnetically charged vector-like fermions coupled to the site $\mathcal{M} < \mathcal{N}$ of the scalar chain. These fermions are responsible for the axion-photon coupling that is, by all accounts, disentangled from the solution of the strong CP problem. In the simplest realization proposed in [49], the γ_\heartsuit QCD model requires the existence of a single pair of vector-like colored fermions in the fundamental representation of $SU(3)_C$ and a single pair of color neutral vector-like fermions with unit hypercharge and singlet under $SU(2)_L$. Under these conditions the axion-photon coupling turns out to be [49]

$$g_{a\gamma\gamma} = \left(\frac{2}{3^{\mathcal{M}-\mathcal{N}}} \right) \frac{\alpha_{\text{em}}}{2\pi f_a}, \quad (67)$$

and the free parameter \mathcal{N} , that is a fundamental parameter of the model, can be changed to make $g_{a\gamma\gamma}$, as promised, arbitrarily large.

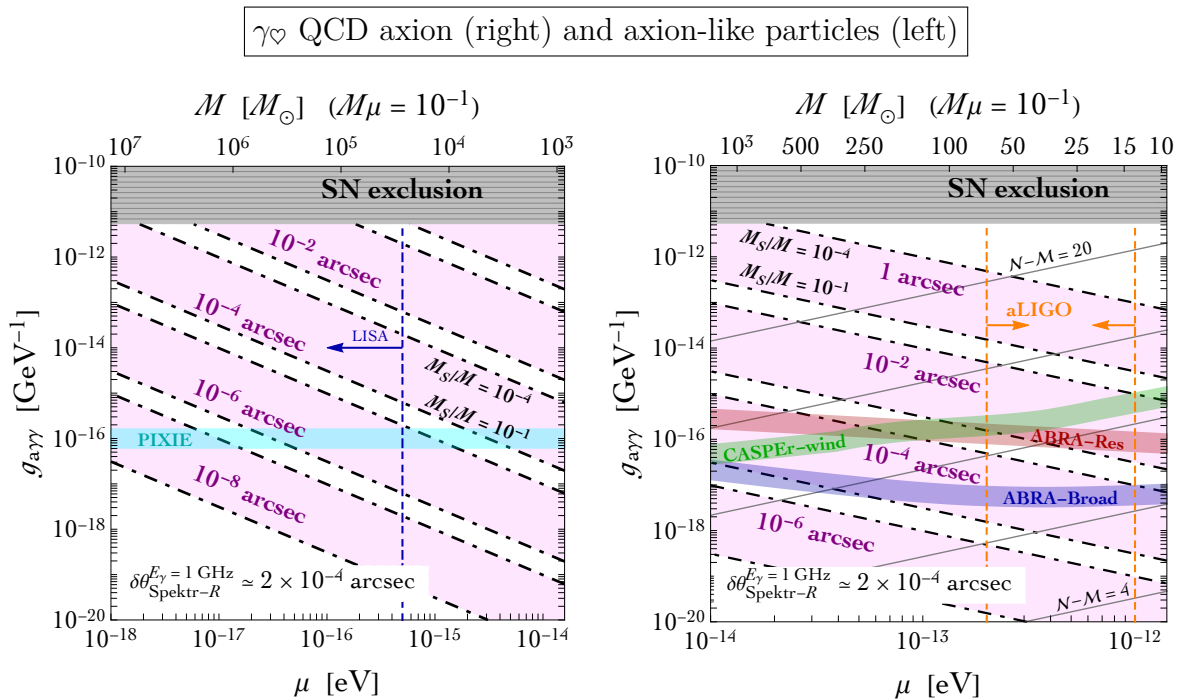


Figure 5: *Right (left) panel. Contours of constant angular splitting for the γ_\heartsuit QCD axion (a generic ALP) as a function of the axion mass μ and the axion-photon coupling $g_{a\gamma\gamma}$. In the case of the γ_\heartsuit QCD axion we show the projected sensitivities of ABRACADABRA [56] and CASPEr-wind [57] together with the mass range that will be explored by the Advanced LIGO gravitational wave interferometer [30, 31]. For a generic ALP, we show a projected limit for the PIXIE/PRISM experiment [58] (see text for details).*

In the right panel of fig. 5 we show the result of our analysis for the γ_\heartsuit QCD axion. We explore the parameter space $(\mu, g_{a\gamma\gamma})$, and we fix $M\mu = 10^{-1}$. We enlarge the axion mass range to the interval $10^{-14} \leq \mu$ [eV] $\leq 10^{-12}$, and we bracket between two vertical dot-dashed orange lines the mass range covered by Advanced LIGO in eq. (66). The above mass range corresponds to the axion decay constant $5.7 \times 10^{18} \lesssim f_a$ [GeV] $\lesssim 5.7 \times 10^{20}$, and in order to

reproduce the observed value of the dark matter relic abundance we need to tune the initial misalignment angle to the values $0.12 \lesssim \theta_{\text{in}} \times 10^5 \text{ [rad]} \lesssim 3.98$. We consider the axion-photon coupling in the range $10^{-20} \leq g_{a\gamma\gamma} \text{ [GeV}^{-1}] \leq 10^{-10}$, and the thin diagonal solid gray lines indicate – in steps of 4, from $\mathcal{N} - \mathcal{M} = 4$ to $\mathcal{N} - \mathcal{M} = 20$ – the values of $g_{a\gamma\gamma}$ as a function of the axion mass for different choices of $\mathcal{N} - \mathcal{M}$ in eq. (67). Contours of constant angle $|\Delta\phi_+ - \Delta\phi_-|$ are shown with dot-dashed diagonal black lines, and the shaded area in magenta corresponds to $10^{-4} \leq M_S/M \leq 10^{-1}$. We fix $E_\gamma = 1 \text{ GHz}$, and – to give an idea about the relevance of the effect – we quote the angular resolution of the Spektr-R radio telescope [52–54], $\delta\theta_{\text{Spektr-R}}^{E_\gamma=1 \text{ GHz}} \simeq 2 \times 10^{-4} \text{ arcsec}$. We postpone to section 4 a more detailed discussion about experimental prospects. The gray area is excluded by SN1987A gamma-ray limit on ultralight axion-like particles, and we use the results of the updated analysis presented in [55]. The plot shows that $|\Delta\phi_+ - \Delta\phi_-| > \delta\theta_{\text{Spektr-R}}^{E_\gamma=1 \text{ GHz}}$ in a wide range of the explored parameter space. We argue that the polarization-dependent lensing computed in section 3 can be relevant for the γ_\heartsuit QCD axion. It is also important to keep in mind that the same region of parameter space is well within the sensitivity range of well-motivated proposals for future experiments. In the right panel of fig. 5 we show the projected sensitivities of ABRACADABRA [56] (considering both the resonant and broadband approach) and CASPER-wind [57]. ABRACADABRA exploits the fact that when axion dark matter encounters a static magnetic field, it sources an effective electric current that follows the magnetic field lines and oscillates at the axion Compton frequency. CASPER-wind considers couplings of the background classical axion field which give rise to observable effects like nuclear electric dipole moment, and axial nucleon and electron moments.

3.3 Axion-like particles

We now turn to discuss the more general case of ALPs. The crucial difference is that there is no *a priori* relationship between the ALP mass μ and the coupling $g_{a\gamma\gamma}$ while in the QCD axion case they are linearly related, and we can therefore treat them as independent parameters. As a result, ultra-light values of μ below those explored in section 3.1 and 3.2 are possible. We show our result in the left panel of fig. 5. In order to provide complementary information with respect to the case of the γ_\heartsuit QCD axion, we consider the mass range $10^{-18} \leq \mu \text{ [eV]} \leq 10^{-14}$. Since $M\mu = 10^{-1}$, this range covers from intermediate-mass to supermassive black holes. As far as the computation of $|\Delta\phi_+ - \Delta\phi_-|$ is concerned, the color code follows what already discussed in section 3.2. We delimit with a vertical dot-dashed blue line the mass range that will be explored by LISA according to the analysis proposed in [30, 31]. We find that $|\Delta\phi_+ - \Delta\phi_-| > \delta\theta_{\text{Spektr-R}}^{E_\gamma=1 \text{ GHz}}$ in a wide range of the explored parameter space, and we argue that the polarization-dependent effect computed in section 3 can be relevant also for a generic ALP. We also show a possible complementarity with future CMB tests of dark matter. The idea is that resonant conversions between CMB photons and light ALPs could result in observable CMB distortions. These resonant conversions depend on the strength of primordial magnetic fields B , and it was shown in [58] that the PIXIE/PRISM experiment [59], according to the

expected sensitivity, has the capabilities to set the limit $g_{a\gamma\gamma}B \lesssim 10^{-16} \text{ GeV}^{-1} \text{ nG}$ for axion mass $\mu \lesssim 10^{-14} \text{ eV}$ (see also [60] for a recent analysis using galaxy clusters). Assuming a strength of primordial magnetic fields close to the current upper limit $B \sim \mathcal{O}(1) \text{ nG}$ [61], we show in cyan the expected limit on $g_{a\gamma\gamma}$ in fig. 5.

4 Discussion and outlook

The setup we have in mind is sketched in fig. 6. We envisage the presence of a black hole surrounded by a scalar cloud in between an astrophysical source emitting linearly polarized light and a ground- or space-based radio telescope. A linearly polarized ray of light is a superposition of right- and left-handed circularly polarized waves (RCP and LCP in fig. 6). By traveling through the scalar cloud, the two components experience a polarization-dependent bending as discussed in the previous section and appendix C. In that event, a polarization-dependent lensing effect would appear in the image captured by the radio telescope.

Is this situation ever possible? In this section, we shall explore in more detail some of the necessary conditions needed to realize this idea.

4.1 General remarks: dual-polarization receiver and VLBI

Consider an electromagnetic wave traveling in the \hat{z} direction. In general, light is elliptically polarized and can be described by means of the electric field

$$\vec{E}_{\text{EP}} = E_x^{(0)} \cos(kz - \omega t) \hat{x} + E_y^{(0)} \cos(kz - \omega t + \delta) \hat{y} \equiv E_x \hat{x} + E_y \hat{y}. \quad (68)$$

The case $\delta = 0$ corresponds to linear polarization whereas the conditions $\delta = \pm\pi/2$, $E_x^{(0)} = E_y^{(0)}$ describe, respectively, a right and left circularly polarized wave. What is relevant for astrophysical observations is light intensity rather than field amplitude. For this reason it is useful to introduce the four Stokes parameters [62]

$$\mathfrak{I} = \langle E_x^2 \rangle + \langle E_y^2 \rangle, \quad \mathfrak{Q} = \langle E_x^2 \rangle - \langle E_y^2 \rangle, \quad \mathfrak{U} = 2\langle E_x E_y \cos \delta \rangle, \quad \mathfrak{V} = 2\langle E_x E_y \sin \delta \rangle, \quad (69)$$

where $\langle \dots \rangle$ denotes a time average over times much larger than $2\pi/\omega$. The parameter \mathfrak{I} measures the intensity of the wave, \mathfrak{Q} and \mathfrak{U} fully describe linear polarization, and \mathfrak{V} corresponds to circularly polarized intensity. In particular, a net right (left) polarization has a positive (negative) \mathfrak{V} .

The radio emission from most bright radio sources arises from synchrotron radiation, and it is linearly polarized. Qualitatively speaking, the reason is the following. The radiation from a single relativistic electron gyrating around a magnetic field is elliptically polarized. For an ensemble of electrons with a smooth distribution of pitch angles the opposite senses of elliptical polarization will cancel out resulting in linearly polarized radiation. This is in particular true in the case of synchrotron emission from Active Galactic Nuclei (AGN) observed at radio frequencies. This is, therefore, the class of astrophysical sources that might be well-suited for our purposes.

Next, we need a radio telescope able to distinguish between left and right polarizations with sufficiently high angular resolution. Polarization-dependent measurements are possible if the instrument is a dual-polarization receiver. In a nutshell, such telescope can be thought as a cross of two dipoles aligned along orthogonal directions. Each of the two dipoles measures the corresponding polarization component and converts it into an electric signal. The signals are auto-correlated and cross-correlated, thus allowing for a reconstruction of the Stokes parameters. What is important to stress is that all four Stokes parameters are actual intensities. This means that they can be used at the level of image analysis in order to reconstruct and visualize the polarization of the observed source. This makes the detection of our effect, at least in principle, possible. Furthermore, we remind that the time average implied in the measurement of the Stokes parameters refers to a time interval Δt much larger than the typical wavelength λ of the observed light. If the condition $\lambda \ll \Delta t \ll \lambda_{\text{Compton}}$ is verified, it could even be possible to detect the time variation of the signal.

Let us now comment about the angular resolution. The angular resolution $\delta\theta$ of a telescope can be calculated from the wavelength of observed radio waves λ and the diameter D of the telescope

$$\delta\theta \approx 2.5 \times 10^5 \frac{\lambda}{D} \text{ arcsec} . \quad (70)$$

To fix ideas, a radio telescope with $D = 65$ m observing radio wavelengths at $E_\gamma = 1$ GHz ($\lambda \approx 0.3$ m) has an angular resolution $\delta\theta \approx 10^3$ arcsec. The angular resolution of a typical radio telescope is, therefore, by far too low to detect the effect computed in section 3. However, it is possible to use multiple radio telescopes at the same time, a technique that is called interferometry. The angular resolution is greatly improved because – by synchronizing and combining observations from all the telescopes of the array, each one equipped by its own atomic clock – one effectively creates a single telescope as large as the distance between the two farthest telescopes. This simple principle lies at the heart of the very-long-baseline interferometry (VLBI) technique, in which a signal from an astronomical radio source is collected from multiple radio telescopes on Earth. VLBI gives angular resolutions of the order of $\delta\theta \approx 10^{-3}$ arcsec or better thus making our speculations about a possible detection more realistic.

A further improvement can be obtained by combining a VLBI array with an additional antenna placed on board of a satellite orbiting the Earth. As a benchmark reference, let us consider the case of the Russian project Spektr-R [52–54]. Spektr-R (formerly RadioAstron) is a dual-polarization receiver space-based 10 meter radio telescope in a highly apogee orbit around the Earth, launched on July 2011. Spektr-R works in conjunction with some of the largest ground-based radio telescopes, and the system forms an interferometric baseline extending up to 3×10^5 km [52–54]. This configuration is able to reach an astonishing angular resolution up to a few millionths of an arcsecond. As a reference, in fig. 5 we quote the typical angular resolution of Spektr-R at $E_\gamma = 1$ GHz, that is about $\delta\theta \approx 2 \times 10^{-4}$ arcsec.

In conclusion, we argue that radio astronomy techniques have the capabilities to detect the polarization-dependent bending discussed in section 3, if realized in Nature. Of course,

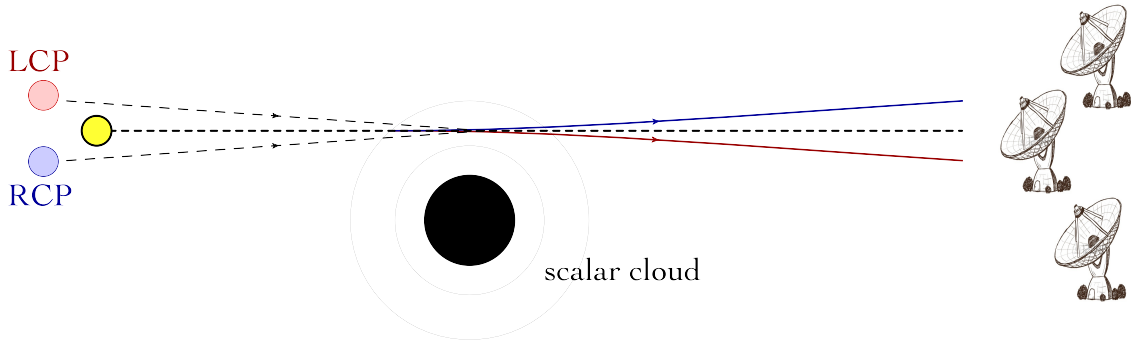


Figure 6: *Sketch of the typical configuration needed to detect the polarization-dependent bending discussed in section 3. An astrophysical radio source like an AGN emits linearly polarized light. Traveling through the axion scalar cloud surrounding a Kerr black hole, the left and right circular components (LCP and RCP) experience different deflection angles thus creating a polarization-dependent lensing that could be observed by an array of radio telescopes using the VLBI technique.*

for the aim of the present work our discussion is purely qualitative, and our intent is that of stimulating the interplay with the radio astronomy community to fully understand the validity of our conclusions.

4.2 Comparison with “background” effects

Scintillation is an optical effect arising when light rays emitted by a compact source pass through a turbulent ionized medium. As far as radio frequencies are concerned, scintillation theory can be applied to the turbulent interstellar medium (ISM) of the Galaxy through angular and pulse broadening of pulsars [63–65], and to the turbulent intergalactic medium (IGM) through quasar observations [66–68].

Interstellar scattering of an extragalactic source of radio waves results in angular broadening. It is, therefore, important to keep in mind the typical size of this effect since it acts as a sort of “background” for the polarization-dependent effect discussed in section 3. If the angular broadening proves to be much larger than the angular splitting $|\Delta\phi_+ - \Delta\phi_-|$, we expect the latter to be clouded by the former.

The size of the broadening of an extragalactic source at redshift z_S due to the IGM – modeled as a thin-screen at redshift z_L with homogeneous Kolmogorov turbulence – is [69]

$$\theta_{\text{scat}} \sim 19.75 \text{ SM}^{3/5} \left(\frac{D_{\text{LS}}}{D_S} \right) \left(\frac{E_\gamma}{1 \text{ GHz}} \right)^{-2.2} (1 + z_L)^{-1.2} 10^{-3} \text{ arcsec} , \quad (71)$$

where D_{LS} (D_S) is the angular diameter distance between the scattering region and the source (between the observer and the source). The angular diameter distance at redshift z is given by the integral

$$D(z) = cH_0^{-1}(1+z)^{-1} \int_0^z \left[\Omega_\Lambda + (1-\Omega)(1+z')^2 + \Omega_m(1+z')^3 + \Omega_r(1+z')^4 \right]^{-1/2} dz' , \quad (72)$$

where H_0 is the Hubble constant, $\Omega = \Omega_\Lambda + \Omega_m + \Omega_r$, and Ω_Λ , Ω_m , Ω_r are, respectively, the ratios of the dark energy density, matter density and radiation density to the critical density of the Universe. We assume Standard Cosmology, with $\Omega = 1$, $\Omega_\Lambda = 0.7$, and $\Omega_r = 0$. In eq. (71) we introduced the short-hand notation $D(z_i) \equiv D_i$. We use $H_0 = 67.8 \pm 0.9$ (km/s)/Mpc [70]. Notice that – defining the angular diameter distance between the observer

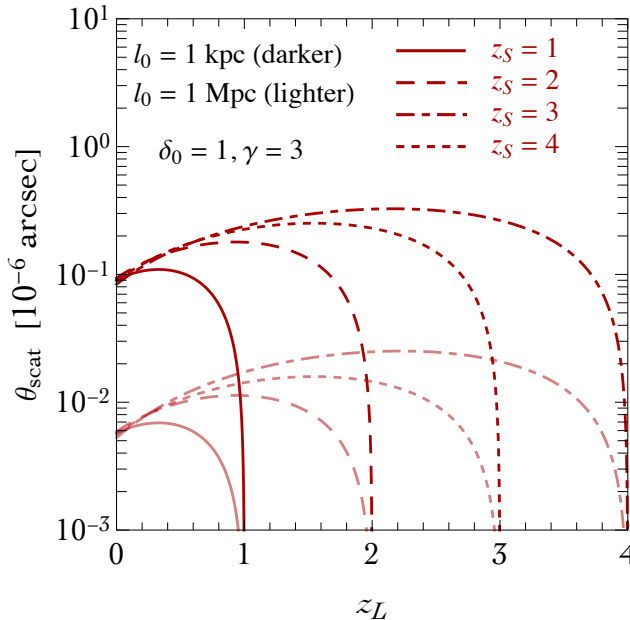


Figure 7: Angular broadening in the IGM at $E_\gamma = 1$ GHz for a screen at redshift z_L .

and the scattering region as D_L – we have in general $D_{LS} \neq D_S - D_L$. In eq. (71), the scattering measure SM encodes the level of turbulence of the IGM, and can be defined as the line-of-sight integral of the spectral coefficient characterizing the power spectrum of electron density fluctuations. Following [69], we have $SM = C_{SM} F n_e^2(z) D_S$. The constant C_{SM} takes the value $C_{SM} = 1.8 \text{ m}^{-20/3} \text{ cm}^6$, $n_e(z)$ is the electron density at redshift z , and the fluctuation parameter is $F = (\zeta \epsilon^2 / \eta) (l_0 / 1 \text{ pc})^{-2/3}$ [63] where l_0 is the outer scale of the turbulence, η is the filling factor of the turbulent medium, ϵ is the variance of the electron density fluctuations within a single cloud, and ζ is a measure of fluctuations in the mean density between clouds. We assume in our estimate $\epsilon \sim \zeta \sim \eta \sim 1$ for all redshifts. This choice implies that the turbulence is fully developed at all redshifts of interest. The outer scale length of turbulence l_0 defines an upper cut off in the size of turbulent structures, and we consider the two benchmark values $l_0 = 1$ kpc, $l_0 = 1$ Mpc. The mean free electron density as a function of the redshift is given by $n_e(z) = \delta_0 x_e(z) n_e(0) (1+z)^\gamma$, where $x_e(z)$ is the ionization fraction, and $n_e(0) = 2.1 \times 10^{-7} \text{ cm}^{-3}$ is the mean free electron density at $z = 0$. We assume a significant ionized fraction, $x_e(z) \sim 1$, for all redshifts of interest. The parameter δ_0 controls possible electron overdensity while $\gamma \sim 3$ for IGM components with constant comoving densities. For simplicity, we take $\delta_0 = 1$. The presence of possible

electron overdensity results in a rescaling of eq. (71) according to the factor $\delta_0^{6/5}$. In fig. 7 we show the angular broadening predicted by eq. (71) at $E_\gamma = 1$ GHz for a screen of ionized medium at redshift z_L . We consider four different source locations, at $z_S = 1, 2, 3, 4$, and two possible choices for the outer scale of the turbulence l_0 (see caption for details). The scattering angle ranges between $10^{-9} \lesssim \theta_{\text{scat}} \lesssim 10^{-7}$ arcsec for $1 \text{ kpc} \lesssim l_0 \lesssim 1 \text{ Mpc}$. We notice that the scattering broadening in the medium hosted by the background source (i.e. considering scattering screens located at $z_L \simeq z_S$) drops to negligible values. Finally, changing the spectral index γ results in a different z_L dependence of the scattering angle, but it does not alter the order of magnitude estimate of the broadening effect.

Given the model-dependence and the astrophysical uncertainties entering in the computation of the angular broadening, no firm conclusion can be established. Nevertheless, the order-of-magnitude estimate proposed in this section keeps alive the hope of detecting the polarization-dependent bending due to a superradiant axion cloud.

4.3 Faraday rotation

Finally, let us close this section with a short discussion about another important effect that is usually relevant in the presence of an optically active medium: Faraday rotation.

Consider a beam of light linearly polarized along the \hat{x} axes

$$\vec{E}_{\text{LP}} = E_0 \cos(kz - \omega t) \hat{x} , \quad \text{with} \quad k = 2\pi/\lambda , \quad \omega = 2\pi\nu . \quad (73)$$

A linearly-polarized wave can be decomposed into a sum of left- and right-circularly polarized waves at the same frequency

$$\vec{E}_{\text{LP}} = \frac{\vec{E}_{\text{RCP}} + \vec{E}_{\text{LCP}}}{2} , \quad \text{with} \quad \vec{E}_{\text{RCP,LCP}} = E_0 [\cos(kz - \omega t) \hat{x} \pm \sin(kz - \omega t) \hat{y}] . \quad (74)$$

Imagine this beam enters a region characterized by the presence of a medium which has slightly different propagation velocities for light with opposite circular polarizations. Upon exiting this region, the left- and right-circular polarization modes have picked up a net phase difference

$$\vec{E}_{\text{RCP,LCP}} = E_0 [\cos(kz - \omega t + \delta_{\text{R,L}}) \hat{x} \pm \sin(kz - \omega t + \delta_{\text{R,L}}) \hat{y}] \quad (75)$$

which causes their sum to still be linearly-polarized, but along a different axis. Indeed the sum $\vec{E}_{\text{LP}} = (\vec{E}_{\text{RCP}} + \vec{E}_{\text{LCP}})/2$

$$\vec{E}_{\text{LP}} = E_0 \left[\cos\left(\frac{\delta_{\text{R}} - \delta_{\text{L}}}{2}\right) \hat{x} + \sin\left(\frac{\delta_{\text{R}} - \delta_{\text{L}}}{2}\right) \hat{y} \right] \cos\left(kz - \omega t + \frac{\delta_{\text{R}} + \delta_{\text{L}}}{2}\right) , \quad (76)$$

describes a plane polarized wave with the polarization direction twisted by an angle $\Delta \equiv (\delta_{\text{R}} - \delta_{\text{L}})/2$ from the x -axis towards the y -axis. This is the Faraday rotation.

The parity violating interaction in eq. (6) may induce Faraday rotation for a beam of light traveling through the axion cloud. We can estimate the size of such effect by considering

a wave traveling a distance $L \sim r_{\text{cloud}}$ in the equatorial plane at radial distance $r \sim r_{\text{max}}$. The change in phase of a circularly polarized mode traveling a distance L is $\delta = L|\vec{k}|$. From eq. (58), and considering the approximation discussed in eq. (64), at the linear order in $g_{a\gamma\gamma}$ we have $|\vec{k}| \approx E_\gamma \mp (g_{a\gamma\gamma}/2)\partial\Phi/\partial t$. We therefore find the estimate $\Delta = L(g_{a\gamma\gamma}/2) \partial\Phi/\partial t|_{r=r_{\text{max}}}$ where for simplicity we assumed a constant cloud (with value fixed at $r = r_{\text{max}}$) along the distance L . We also neglected the trigonometric factor that is responsible for the rotation of the cloud. This estimate should be therefore considered as an order-of-magnitude upper limit for the effect. For the QCD axion and for a generic ALP we find

$$\Delta_{\text{QCD}} = 2 \times 10^{-5} \left(\frac{E}{N} - 1.92 \right) \left(\frac{\mu}{10^{-12} \text{ eV}} \right) \left(\frac{M_S/M}{0.1} \right)^{1/2} \left(\frac{M\mu}{0.1} \right) \text{ rad} , \quad (77)$$

$$\Delta_{\text{ALP}} = 10 \left(\frac{g_{a\gamma\gamma}}{10^{-16} \text{ GeV}^{-1}} \right) \left(\frac{M_S/M}{0.1} \right)^{1/2} \left(\frac{M\mu}{0.1} \right) \text{ rad} . \quad (78)$$

Our Galaxy is full of ionized hot gas, and is simultaneously permeated by a large-scale magnetic field. The Faraday effect due to this plasma is observed in the polarized signal from radio pulsars within our Galaxy, and on all extragalactic radio sources. The subtlety is that we do not know the original plane of polarization. As a consequence, the effect is almost always studied as a function of frequency. In this case the Faraday rotation has the simple form $\Delta = \text{RM} \lambda^2$, where λ is the wavelength of the observed light and RM is the rotation measure which in general depends on the interstellar magnetic field and the number density of electrons along the propagation path. In the idealized case, one can determine the RM by measuring Δ at different wavelengths, and then performing a linear fit. From the value of RM, one can in turn try to decrypt the physical conditions along the lines of sight.

The effect proposed in eqs. (77, 78) does not feature any energy dependence. Without knowing the original direction of polarization, therefore, a possible detection of this effect seems hopeless. One possibility is to exploit the time-dependence of the signal, similar to the one discussed in the right panel of fig. 4, that should give rise to a time-dependent oscillating effect with period set by $1/\mu$.

Another interesting aspect is to consider as a source of light the accretion disk surrounding the black hole (instead of a distant source as done in section 4). Gravitational and frictional forces compress and raise the temperature of the material in the disk, thus causing the emission of electromagnetic radiation that should travel through the axion cloud before escaping.

We do not explore further such possibilities, and we postpone a more detailed investigation to future work.

5 Conclusions

Black holes were long considered a mathematical curiosity rather than a true prediction of General Relativity realized in Nature. After the first direct detection of gravitational waves and the first observation of a binary black hole merger [71], the possibility to turn black holes

from theoretical laboratories to real “particle detectors” has never been nearer than today. However paradoxical this may seem, black holes could help us in finding one of the most theoretically motivated, but experimentally elusive, particle: The axion. This is because a rotating black hole can host an axion cloud – fed by superradiant instability at the expense of the black hole rotational energy – surrounding it. Up to now the properties of such system were studied only considering gravitational interactions. This is a limitation since any boson with the same mass, irrespective of its particle physics origin, displays the same superradiant physics as long as gravitational interactions are concerned.

In this paper we investigated the possible consequences of the parity-violating coupling of the axion with an electromagnetic field in the context of black hole superradiance. The key idea is that the axion cloud surrounding a Kerr black hole behaves like an optically active medium, and a ray of light experiences a polarization-dependent bending traveling through it. Motivated by this picture, we computed the polarization-dependent lensing caused by this phenomenon considering the QCD axion, the photo-philic QCD axion, and a generic ALP. We discussed the experimental setup that is needed to detect such effect, focusing on the radio observation of a linearly polarized astrophysical source like an AGN. We argued that a VLBI array of radio telescopes has the capability to detect the polarization-dependent bending effect caused by the axion cloud surrounding a Kerr black hole, and we delimited the parameter space in which this is relevant in conjunction with other experimental axion searches.

Acknowledgments

We thank Diego Blas, Chris Done, Carlos Herdeiro, Jun Hou, Luca Di Luzio and Sergey Sibiryakov for discussions, and Paolo Pani for valuable comments on a preliminary version of this manuscript.

A Radial eigenfunctions and rotating axion cloud

The radial eq. (11) admits two well-defined limits in the near- and far-horizon region. In the far-horizon region, defined by the condition $r \gg M$, $\Delta \simeq r^2(1 - 2M/r)$, the radial equation reduces to

$$\frac{d^2(\tilde{r}R_{\text{far}})}{d\tilde{r}^2} + \left[-\frac{1}{4} + \frac{l+n+1}{\tilde{r}} - \frac{l(l+1)}{\tilde{r}^2} \right] \tilde{r}R_{\text{far}} = 0 , \quad (79)$$

with R_{far} function of \tilde{r} defined accordingly to eq. (23). This is the same equation describing an electron in the hydrogen atom, thus enforcing the analogy with Quantum Mechanics. Eq. (79) can be solved in terms of confluent hypergeometric function

$$R_{\text{far}}(\tilde{r}) = \tilde{r}^l e^{-\tilde{r}/2} {}_1F_1(l+1-\nu; 2l+2; \tilde{r}) , \quad (80)$$

with $\nu = l + n + 1$ the principal quantum number. The confluent hypergeometric function is given in terms of the Laguerre polynomial by

$$L_n^m(x) = \frac{(m+n)!}{m!n!} {}_1F_1(-n; m+1; x), \quad (81)$$

and eq. (80) reproduces the radial function used in eq. (23) that is, therefore, strictly valid only in the far-horizon limit. In the near-horizon region, defined by $0 < r - r_+ \ll (l/M\mu)^2 M$, the radial equation is solved by [15]

$$R_{\text{near}}(r) = \left(\frac{r - r_+}{r - r_-} \right)^{-iP} {}_2F_1 \left(-l; l+1; 1+2iP; \frac{r - r_-}{r_+ - r_-} \right), \quad P \equiv 2r_+ \left(\frac{\omega - m\Omega_+}{r_+ - r_-} \right), \quad (82)$$

where the angular velocity of the black hole horizon is $\Omega_H = \tilde{a}/2r_+$.

The eigenvalue problem for the radial equation can be solved by means of the continued fraction method championed in [72] (see also [73], and [74] for a pedagogical review about modern black hole perturbation theory). In a nutshell, we look for a radial solution of the form

$$R(r) = (r - r_+)^{-i\sigma} (r - r_-)^{i\sigma + \chi - 1} e^{-r\sqrt{\mu^2 - \omega^2}} \sum_{n=0}^{\infty} a_n \left(\frac{r - r_+}{r - r_-} \right)^n, \quad (83)$$

with

$$\sigma = \frac{2Mr_+}{r_+ - r_-} (\omega - m\Omega_H), \quad \chi = \frac{M(2\omega^2 - \mu^2)}{\sqrt{\mu^2 - \omega^2}}. \quad (84)$$

Note that this ansatz correctly describes the characteristic asymptotic behavior of bound states. Using this expression for $R(r)$, the radial equation returns a three-term recurrence relation for the coefficients a_n that can be solved only for particular values of $\omega = \omega_R + i\omega_I$. These are the eigenfrequencies describing bound states. We implement numerically the continued fraction method, and we show in fig. 8 the values of ω_R (left panel) and ω_I (right panel) obtained by solving the eigenvalue problem for the radial equation. In the small $M\mu$ limit, the agreement with the approximation used in eqs. (19,20) is evident. Having computed the bound state frequencies, the full radial eigenfunction can be obtained from eq. (83). We show our numerical solution in fig. 9, and we comment about the comparison with the far-horizon approximation (see caption for details).

Finally, it is possible to reconstruct the full solution of the Klein-Gordon equation in eq. (9) by including the angular- and time-dependent part. For completeness, we show the full solution in the equatorial plane in fig. 10 (see caption for details).

B Modified dispersion relation

In this appendix we derive the dispersion relation in eq. (57). From the Lagrangian density

$$\mathcal{L} = -\frac{1}{4} F_{\mu\nu} F^{\mu\nu} - \frac{g_{a\gamma\gamma}}{2} (\partial_\mu \Phi) A_\nu \tilde{F}^{\mu\nu}, \quad (85)$$

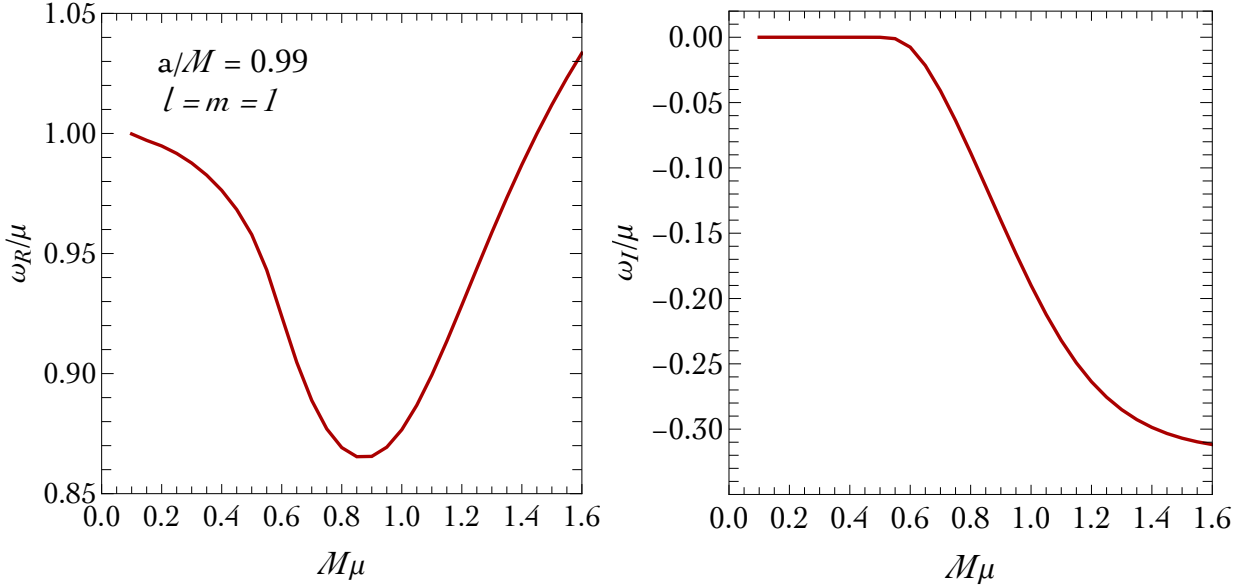


Figure 8: *Real and imaginary part (left and right panel, respectively) of the bound state frequencies for a scalar field in a Kerr background, as a function of the dimensionless parameter $M\mu$. We fix the spin parameter $a/M = 0.99$, and we focus on the eigenmode with $l = m = 1$. We solved numerically eq. (11), and we used the Leaver's method to obtain the bound state frequencies when $M\mu \sim 1$ [73].*

we extract the Euler-Lagrange equations of motion $[g^{\mu\nu}\square - g_{\alpha\gamma\gamma}\epsilon^{\mu\nu\alpha\beta}(\partial_\alpha\Phi)\partial_\beta]A_\nu(x) = 0$ which, in Fourier space, give

$$[g^{\mu\nu}k^2 + ig_{\alpha\gamma\gamma}\epsilon^{\mu\nu\alpha\beta}(\partial_\alpha\Phi)k_\beta]\tilde{A}_\nu(k) \equiv K^{\mu\nu}\tilde{A}_\nu(k) = 0. \quad (86)$$

In eq. (86) we neglected the second derivative term proportional to $g_{\alpha\gamma\gamma}(\partial_\mu\partial_\rho\Phi)A_\sigma\epsilon^{\rho\sigma\mu\nu}$, in analogy with what discussed in section 3. We introduce the short-hand notation $\eta_\alpha \equiv g_{\alpha\gamma\gamma}(\partial_\alpha\Phi)$. In order to solve eq. (86) we define the operator $S^\mu_\nu \equiv \epsilon^{\lambda\mu\alpha\beta}\eta_\alpha k_\beta \epsilon_{\lambda\nu\rho\sigma}\eta^\rho k^\sigma$. The Levi-Civita contraction property

$$\epsilon_{i_1, \dots, i_k, i_{k+1}, \dots, i_n} \epsilon^{i_1, \dots, i_k, j_{k+1}, \dots, j_n} = (-1)^k k! \delta_{i_{k+1}, \dots, i_n}^{j_{k+1}, \dots, j_n}, \quad \text{with } \delta_{\nu_1, \dots, \nu_p}^{\mu_1, \dots, \mu_p} \equiv \begin{vmatrix} \delta_{\nu_1}^{\mu_1} & \dots & \delta_{\nu_p}^{\mu_1} \\ \vdots & \ddots & \vdots \\ \delta_{\nu_1}^{\mu_p} & \dots & \delta_{\nu_p}^{\mu_p} \end{vmatrix}, \quad (87)$$

gives the explicit expression

$$S^{\mu\nu} = g^{\mu\nu} [(\eta \cdot k)^2 - \eta^2 k^2] - \eta \cdot k (\eta^\mu k^\nu + \eta^\nu k^\mu) + k^2 \eta^\mu \eta^\nu + \eta^2 k^\mu k^\nu, \quad (88)$$

with the following properties

$$S^{\mu\nu} k_\nu = S^{\mu\nu} \eta_\nu = 0, \quad S \equiv S^\mu_\mu = 2 [(\eta \cdot k)^2 - \eta^2 k^2], \quad S^{\mu\nu} S_{\nu\lambda} = \frac{S}{2} S^\mu_\lambda. \quad (89)$$

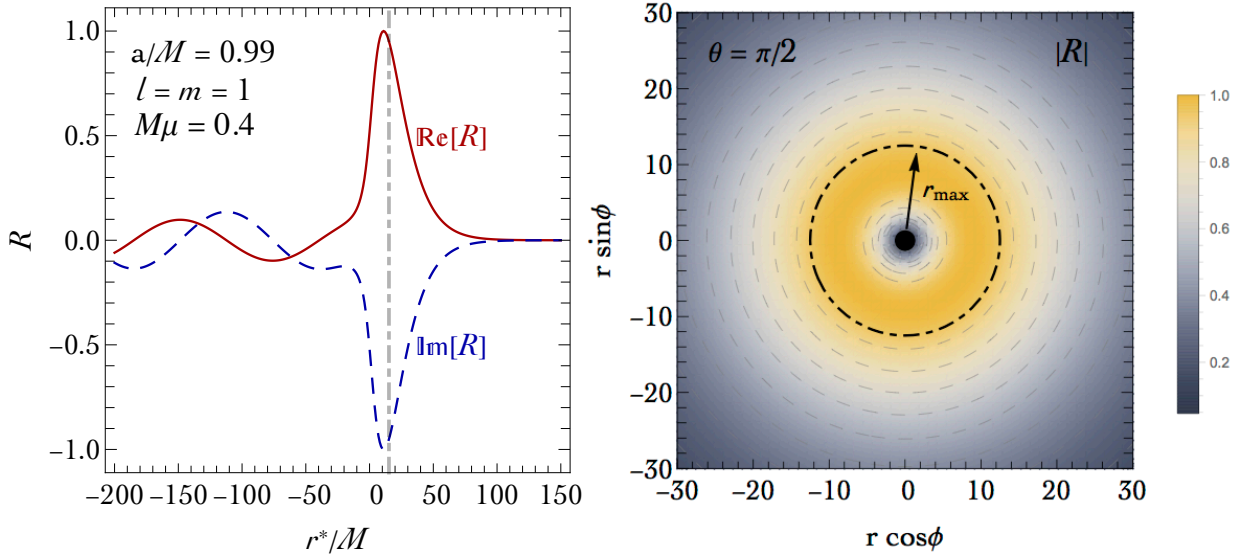


Figure 9: *Left panel.* Real (red, solid line) and imaginary (blue, dashed line) part of the radial eigenfunction R with $l = m = 1$ as a function of the tortoise coordinate r^* obtained numerically using the Leaver's method [73]. For comparison, the vertical gray dot-dashed line indicates at $r^*/M \simeq 15.2$ indicates the position of $\tilde{r}_{\max} = 2$ in terms of the tortoise coordinate. *Right panel.* Density plot of the absolute value $|R|$ (arbitrarily normalized to 1 at the maximum) in the equatorial plane $\theta = \pi/2$. The black dot-dashed circle indicates the location of $\tilde{r}_{\max} = 2$ obtained using the analytical approximation in eq. (23).

We can define the two projectors

$$\mathcal{P}_{\pm}^{\mu\nu} \equiv \frac{S^{\mu\nu}}{S} \mp \frac{i}{\sqrt{2}S} \epsilon^{\mu\nu\alpha\beta} \eta_{\alpha} k_{\beta} . \quad (90)$$

This is a good definition, since we have the following properties

$$\mathcal{P}_{\pm}^{\mu\lambda} \mathcal{P}_{\pm\lambda\nu} = \mathcal{P}_{\pm}^{\mu}_{\nu} , \quad \mathcal{P}_{\pm}^{\mu\lambda} \mathcal{P}_{\mp\lambda\nu} = 0 . \quad (91)$$

Furthermore, $\mathcal{P}_{\pm}^{\mu\nu} k_{\nu} = \mathcal{P}_{\pm}^{\mu\nu} \eta_{\nu} = 0$, $g_{\mu\nu} \mathcal{P}_{\pm}^{\mu\nu} = 1$, and $\mathcal{P}_{+}^{\mu\nu} + \mathcal{P}_{-}^{\mu\nu} = 2S^{\mu\nu}/S$. The operator in eq. (86) becomes

$$K^{\mu\nu} = g^{\mu\nu} k^2 + \sqrt{\frac{S}{2}} (\mathcal{P}_{-}^{\mu\nu} - \mathcal{P}_{+}^{\mu\nu}) . \quad (92)$$

We now have all the ingredients to derive a dispersion relation from eq. (86). We start from a space-like unit vector, for example $\varepsilon = (0, i, 1, 0)/\sqrt{2}$. We then define the two projections $\tilde{\varepsilon}_{\pm}^{\mu} \equiv \mathcal{P}_{\pm}^{\mu\nu} \varepsilon_{\nu}$. From the properties of the projectors it follows that

$$K^{\mu\nu} \tilde{\varepsilon}_{\pm\nu} = \left[k^2 \mp \sqrt{\frac{S}{2}} \right] \tilde{\varepsilon}_{\pm}^{\mu} . \quad (93)$$

Therefore, $\tilde{A}^{\mu} = \tilde{\varepsilon}_{\pm}^{\mu}$ is a solution of eq. (86) if and only if $k^2 = \pm\sqrt{S/2}$, or

$$k^4 + \eta^2 k^2 = (\eta \cdot k)^2 , \quad (94)$$

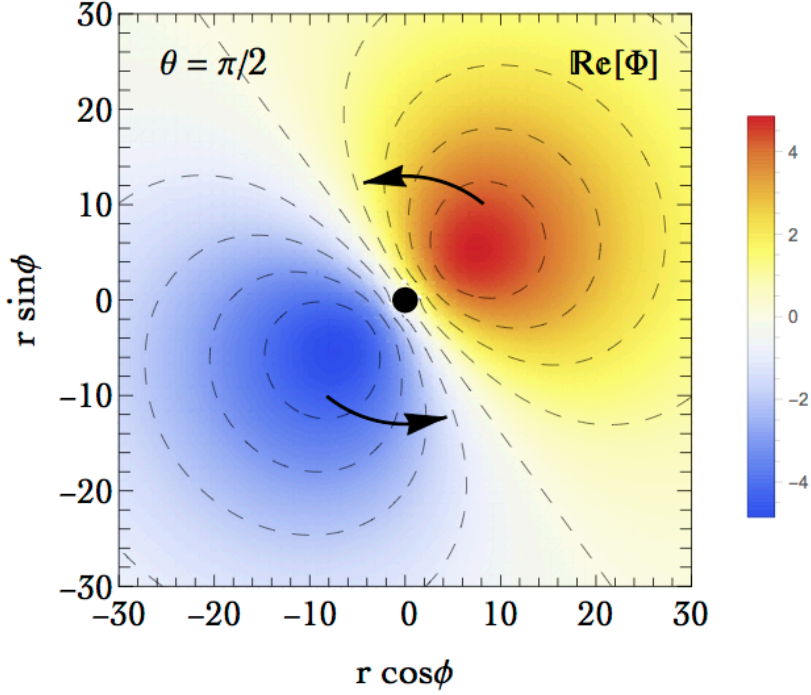


Figure 10: Density plot of the axion cloud $\text{Re}[\Phi] = \text{Re} \left[e^{im\phi} S_{lm}(\theta) e^{-i\omega t} R_{nl}(r) \right]$ with $n = 0$, $l = m = 1$ in the equatorial plane. We consider the explicit case with $a/M = 0.99$, $M\mu = 0.4$, and we take for reference $t = 0$. As time passes by, the axion cloud rotates anti-clockwise in the direction of the black arrows. The period is $T = 2\pi/\omega_R$.

that is the modified dispersion relation presented in eq. (57). Since the limit $g_{a\gamma\gamma} \rightarrow 0$ should recover the standard parity-invariant propagation in which there is no difference in the physical properties of a right- and a left-handed circularly polarized electromagnetic wave, it is natural to identify the two distinct solutions arising in the case $g_{a\gamma\gamma} \neq 0$ as the two different circular polarizations.

C Equation for the photon orbit

Let us start from eq. (60) in Schwarzschild background

$$\left(\frac{dr}{d\xi} \right)^2 = E_\gamma^2 - \frac{L^2}{r^2} \left(1 - \frac{2M}{r} \right) \mp g_{a\gamma\gamma} E_\gamma \frac{\partial \Phi}{\partial t}. \quad (95)$$

The equation for the photon orbit is given by

$$\frac{d\phi}{dr} = \frac{d\phi}{d\xi} \frac{d\xi}{dr} = \pm \frac{1}{r^2 \sqrt{\frac{E_\gamma^2}{L^2} \left(1 \mp \frac{g_{a\gamma\gamma}}{E_\gamma} \frac{\partial \Phi}{\partial t} \right) - \frac{1}{r^2} \left(1 - \frac{2M}{r} \right)}}, \quad (96)$$

where the minus (plus) sign corresponds to incoming (outgoing) light rays.

The angle ϕ is defined to be $\phi = 0$ for incoming light at infinite distance from the black hole. Light traveling in straight line will have $\phi = \pi$ in the opposite outgoing limit. In order to compute the deflection angle we consider the setup illustrated in fig. 11. We follow the standard computation of gravitational lensing. The distance of closest approach r_0 of the light ray is defined by means of the condition $dr/d\xi = 0$. From eq. (95) we find

$$\frac{E_\gamma^2}{L^2} = \frac{1 - 2M/r_0}{r_0^2 \left[1 \mp a(E_\gamma, r_0, \frac{\pi + \Delta\phi_\pm}{2}) \right]}, \quad \text{with} \quad a(E_\gamma, r, \phi) \equiv \frac{g_{a\gamma\gamma}}{E_\gamma} \frac{\partial\Phi}{\partial t} \Big|_{r,\phi}. \quad (97)$$

The distance of closest approach defines the angles $\Delta\phi_\pm$ as one can see from fig. 11. Note that $E_\gamma^2/L^2 = 1/b^2$ defines the impact parameter b . If we fix r_0 to be the same for both left- and right-handed circularly polarized waves we have two different values for the impact parameter, as illustrated in fig. 11. Alternatively, one can fix the impact parameter but in this case the distance of closest approach will differ between the two polarizations. We can

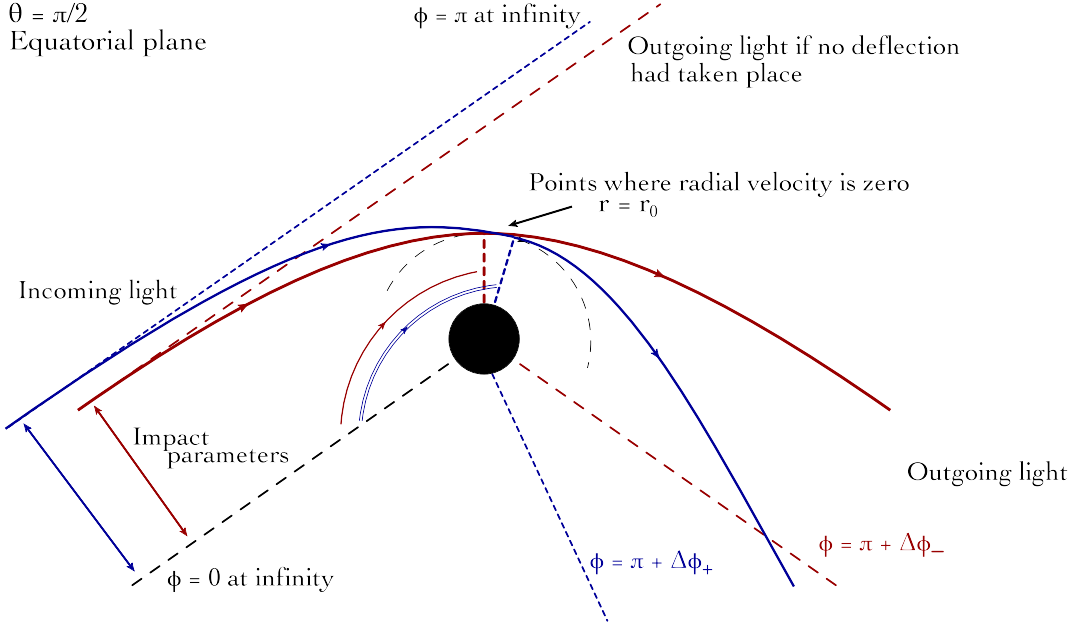


Figure 11: Deflection of a ray of light in the gravitational field of a black hole with mass M . The dashed arc of circumference represents the points at distance $r = r_0$ from the black hole center.

now use the condition in eq. (97) into eq. (96). For incoming light rays, we find

$$\frac{d\phi}{dr} = - \frac{1}{r^2 \sqrt{\frac{1}{r_0^2} \frac{[1 \mp a(E_\gamma, r, \phi)]}{[1 \mp a(E_\gamma, r_0, \frac{\pi + \Delta\phi_\pm}{2})]} \left(1 - \frac{2M}{r_0} \right) - \frac{1}{r^2} \left(1 - \frac{2M}{r} \right)}}}. \quad (98)$$

This equation must be integrated between $r = \infty$ and $r = r_0$ in order to obtain the deflection angle for incoming light rays. The final deflection angle, $\pi + \Delta\phi_\pm$, is obtained by adding the

corresponding integration – in the interval between $r = r_0$ and $r = \infty$ – for outgoing light rays, as illustrated in fig. 11.

We can use the following approximation in eq. (98). In our computation we take the distance of closest approach to be $r_0 = r_{\max}$. Furthermore, we introduce the dimensionless variable $x \equiv r/M$, and we find

$$\frac{d\phi}{dx} = -\frac{1}{x^2 \sqrt{\frac{1}{x_{\max}^2} - \frac{[1 \mp a(E_\gamma, x, \phi)]}{[1 \mp a(E_\gamma, x_{\max}, \frac{\pi + \Delta\phi_{\mp})]}]} \left(1 - \frac{2}{x_{\max}}\right) - \frac{1}{x^2} \left(1 - \frac{2}{x}\right)}. \quad (99)$$

The flat space limit is

$$\frac{d\phi}{dx} = -\frac{1}{x^2 \sqrt{\frac{1}{x_{\max}^2} - \frac{[1 \mp a(E_\gamma, x, \phi)]}{[1 \mp a(E_\gamma, x_{\max}, \frac{\pi + \Delta\phi_{\mp})]}]} - \frac{1}{x^2}}. \quad (100)$$

Let us now expand the right-hand side for small a . We find

$$\frac{d\phi}{dx} = -\frac{1}{x^2 \sqrt{\frac{1}{x_{\max}^2} - \frac{1}{x^2}}} \mp \frac{a(E_\gamma, x, \phi) - a(E_\gamma, x_{\max}, \frac{\pi + \Delta\phi_{\mp})}{2}}{2x^2 x_{\max}^2 \left(\frac{1}{x_{\max}^2} - \frac{1}{x^2}\right)^{3/2}}. \quad (101)$$

The first term reproduces the trivial flat space limit, and the integration between $x = \infty$ and $x = x_{\max}$ gives the angle $\phi = \pi/2$ corresponding to outgoing light with no deflection, as illustrated in fig. 11. Since by definition $\Delta\phi_{\pm} \sim \mathcal{O}(g_{a\gamma\gamma})$, at the first order in the coupling $g_{a\gamma\gamma}$ we can write

$$\frac{d\phi}{dx} = -\frac{1}{x^2 \sqrt{\frac{1}{x_{\max}^2} - \frac{1}{x^2}}} \mp \frac{a(E_\gamma, x, \phi) - a(E_\gamma, x_{\max}, \frac{\pi}{2})}{2x^2 x_{\max}^2 \left(\frac{1}{x_{\max}^2} - \frac{1}{x^2}\right)^{3/2}}, \quad (102)$$

that is the equation for the photon orbit that we solved in section 3.

References

- [1] R. Brito, V. Cardoso and P. Pani, “*Superradiance : Energy Extraction, Black-Hole Bombs and Implications for Astrophysics and Particle Physics*,” Lect. Notes Phys. **906**, pp.1 (2015) [[arXiv:1501.06570](#) [gr-qc]].
- [2] W. H. Press and S. A. Teukolsky, “*Floating Orbits, Superradiant Scattering and the Black-hole Bomb*,” Nature **238**, 211 (1972).
- [3] W. H. Press and S. A. Teukolsky, “*Perturbations of a Rotating Black Hole. II. Dynamical Stability of the Kerr Metric*,” Astrophys. J. **185**, 649 (1973).
- [4] S. A. Teukolsky and W. H. Press, “*Perturbations of a rotating black hole. III - Interaction of the hole with gravitational and electromagnetic radiation*,” Astrophys. J. **193**, 443 (1974).
- [5] T. Damour, N. Deruelle and R. Ruffini, “*On Quantum Resonances in Stationary Geometries*,” Lett. Nuovo Cim. **15**, 257 (1976).
- [6] T. J. M. Zouros and D. M. Eardley, “*Instabilities Of Massive Scalar Perturbations Of A Rotating Black Hole*,” Annals Phys. **118**, 139 (1979).
- [7] S. L. Detweiler, “*Klein-gordon Equation And Rotating Black Holes*,” Phys. Rev. D **22**, 2323 (1980).
- [8] R. Penrose and R. M. Floyd, “*Extraction of rotational energy from a black hole*,” Nature **229**, 177 (1971).
- [9] V. Cardoso, P. Pani and T. T. Yu, “*Superradiance in rotating stars and pulsar-timing constraints on dark photons*,” Phys. Rev. D **95**, no. 12, 124056 (2017) [[arXiv:1704.06151](#) [gr-qc]].
- [10] P. Pani, V. Cardoso, L. Gualtieri, E. Berti and A. Ishibashi, “*Black hole bombs and photon mass bounds*,” Phys. Rev. Lett. **109**, 131102 (2012) [[arXiv:1209.0465](#) [gr-qc]].
- [11] M. Baryakhtar, R. Lasenby and M. Teo, “*Black Hole Superradiance Signatures of Ultra-light Vectors*,” Phys. Rev. D **96**, no. 3, 035019 (2017) [[arXiv:1704.05081](#) [hep-ph]].
- [12] R. Brito, V. Cardoso and P. Pani, “*Massive spin-2 fields on black hole spacetimes: Instability of the Schwarzschild and Kerr solutions and bounds on the graviton mass*,” Phys. Rev. D **88**, no. 2, 023514 (2013) [[arXiv:1304.6725](#) [gr-qc]].
- [13] J. E. McClintock, R. Narayan and J. F. Steiner, “*Black Hole Spin via Continuum Fitting and the Role of Spin in Powering Transient Jets*,” Space Sci. Rev. **183**, 295 (2014) [[arXiv:1303.1583](#) [astro-ph.HE]].
- [14] C. S. Reynolds, “*Measuring Black Hole Spin using X-ray Reflection Spectroscopy*,” Space Sci. Rev. **183**, no. 1-4, 277 (2014) [[arXiv:1302.3260](#) [astro-ph.HE]].
- [15] A. Arvanitaki and S. Dubovsky, “*Exploring the String Axiverse with Precision Black Hole Physics*,” Phys. Rev. D **83** (2011) 044026 [[arXiv:1004.3558](#) [hep-th]].
- [16] A. Arvanitaki, S. Dimopoulos, S. Dubovsky, N. Kaloper and J. March-Russell, “*String Axiverse*,” Phys. Rev. D **81**, 123530 (2010) [[arXiv:0905.4720](#) [hep-th]].

- [17] See, e.g.: G. Carosi, A. Friedland, M. Giannotti, M. J. Pivovarov, J. Ruz and J. K. Vogel, “*Probing the axion-photon coupling: phenomenological and experimental perspectives. A snowmass white paper,*” [arXiv:1309.7035](#) [hep-ph].
- [18] “*Kerr’s solution has also surpassing theoretical interest: it has many properties that have the aura of the miraculous about them.*” S. Chandrasekhar in “General Relativity: An introductory survey.” Cambridge University Press, 1979.
- [19] B. Carter, “*Global structure of the Kerr family of gravitational fields,*” Phys. Rev. **174**, 1559 (1968).
- [20] M. Walker and R. Penrose, “*On quadratic first integrals of the geodesic equations for type [22] spacetimes,*” Commun. Math. Phys. **18**, 265 (1970).
- [21] E. Berti, V. Cardoso and M. Casals, “*Eigenvalues and eigenfunctions of spin-weighted spheroidal harmonics in four and higher dimensions,*” Phys. Rev. D **73**, 024013 (2006) Erratum: [Phys. Rev. D **73**, 109902 (2006)] [[gr-qc/0511111](#)].
- [22] H. Yoshino and H. Kodama, “*Gravitational radiation from an axion cloud around a black hole: Superradiant phase,*” PTEP **2014**, 043E02 (2014) [[arXiv:1312.2326](#) [gr-qc]].
- [23] D. N. Page and K. S. Thorne, “*Disk-Accretion onto a Black Hole. Time-Averaged Structure of Accretion Disk,*” Astrophys. J. **191**, 499 (1974).
- [24] K. S. Thorne, “*Disk accretion onto a black hole. 2. Evolution of the hole.,*” Astrophys. J. **191**, 507 (1974).
- [25] J. M. Bardeen, “*Kerr Metric Black Holes,*” Nature **226**, 64 (1970).
- [26] R. Brito, V. Cardoso and P. Pani, “*Black holes as particle detectors: evolution of superradiant instabilities,*” Class. Quant. Grav. **32**, no. 13, 134001 (2015) [[arXiv:1411.0686](#) [gr-qc]].
- [27] A. Arvanitaki, M. Baryakhtar and X. Huang, “*Discovering the QCD Axion with Black Holes and Gravitational Waves,*” Phys. Rev. D **91**, no. 8, 084011 (2015) [[arXiv:1411.2263](#) [hep-ph]].
- [28] V. P. Frolov and I. D. Novikov, “*Black hole physics: Basic concepts and new developments,*” (Fundamental theories of physics. 96).
- [29] A. D. Dolgov, I. B. Khriplovich and V. I. Zakharov, “*Chiral Boson Anomaly in a Gravitational Field,*” JETP Lett. **45** (1987) 651.
- [30] R. Brito, S. Ghosh, E. Barausse, E. Berti, V. Cardoso, I. Dvorkin, A. Klein and P. Pani, “*Stochastic and resolvable gravitational waves from ultralight bosons,*” Phys. Rev. Lett. **119**, no. 13, 131101 (2017) [[arXiv:1706.05097](#) [gr-qc]].
- [31] R. Brito, S. Ghosh, E. Barausse, E. Berti, V. Cardoso, I. Dvorkin, A. Klein and P. Pani, “*Gravitational wave searches for ultralight bosons with LIGO and LISA,*” Phys. Rev. D **96**, no. 6, 064050 (2017) [[arXiv:1706.06311](#) [gr-qc]].
- [32] H. Yoshino and H. Kodama, “*Bosenova collapse of axion cloud around a rotating black hole,*” Prog. Theor. Phys. **128**, 153 (2012) [[arXiv:1203.5070](#) [gr-qc]].

- [33] M. J. Bowick, S. B. Giddings, J. A. Harvey, G. T. Horowitz and A. Strominger, “*Axionic Black Holes and a Bohm-Aharonov Effect for Strings,*” Phys. Rev. Lett. **61**, 2823 (1988).
- [34] K. M. Lee and E. J. Weinberg, “*Charge black holes with scalar hair,*” Phys. Rev. D **44**, 3159 (1991).
- [35] B. A. Campbell, N. Kaloper and K. A. Olive, “*Axion hair for dyon black holes,*” Phys. Lett. B **263**, 364 (1991).
- [36] B. A. Campbell, N. Kaloper and K. A. Olive, “*Classical hair for Kerr-Newman black holes in string gravity,*” Phys. Lett. B **285**, 199 (1992).
- [37] M. Reuter, “*A Mechanism generating axion hair for Kerr black holes,*” Class. Quant. Grav. **9**, 751 (1992).
- [38] G. Grilli di Cortona, E. Hardy, J. Pardo Vega and G. Villadoro, “*The QCD axion, precisely,*” JHEP **1601**, 034 (2016) [[arXiv:1511.02867](#) [hep-ph]].
- [39] C. Patrignani *et al.* [Particle Data Group], “*Review of Particle Physics,*” Chin. Phys. C **40**, no. 10, 100001 (2016).
- [40] A. R. Zhitnitsky, “*On Possible Suppression of the Axion Hadron Interactions. (In Russian),*” Sov. J. Nucl. Phys. **31**, 260 (1980) [Yad. Fiz. **31**, 497 (1980)].
- [41] M. Dine, W. Fischler and M. Srednicki, “*A Simple Solution to the Strong CP Problem with a Harmless Axion,*” Phys. Lett. **104B**, 199 (1981).
- [42] J. E. Kim, “*Weak Interaction Singlet and Strong CP Invariance,*” Phys. Rev. Lett. **43**, 103 (1979).
- [43] M. A. Shifman, A. I. Vainshtein and V. I. Zakharov, “*Can Confinement Ensure Natural CP Invariance of Strong Interactions?,*” Nucl. Phys. B **166**, 493 (1980).
- [44] L. Di Luzio, F. Mescia and E. Nardi, “*Redefining the Axion Window,*” Phys. Rev. Lett. **118**, no. 3, 031801 (2017) [[arXiv:1610.07593](#) [hep-ph]].
- [45] D. Harari and P. Sikivie, “*Effects of a Nambu-Goldstone boson on the polarization of radio galaxies and the cosmic microwave background,*” Phys. Lett. B **289**, 67 (1992).
- [46] S. M. Carroll, G. B. Field and R. Jackiw, “*Limits on a Lorentz and Parity Violating Modification of Electrodynamics,*” Phys. Rev. D **41**, 1231 (1990).
- [47] R. Alonso and A. Urbano, “*Wormholes and masses for Goldstone bosons,*” [arXiv:1706.07415](#) [hep-ph].
- [48] R. Kallosh, A. D. Linde, D. A. Linde and L. Susskind, “*Gravity and global symmetries,*” Phys. Rev. D **52**, 912 (1995) [[hep-th/9502069](#)].
- [49] M. Farina, D. Pappadopulo, F. Rompineve and A. Tesi, “*The photo-philic QCD axion,*” JHEP **1701**, 095 (2017) [[arXiv:1611.09855](#) [hep-ph]].
- [50] K. Choi and S. H. Im, “*Realizing the relaxion from multiple axions and its UV completion with high scale supersymmetry,*” JHEP **1601**, 149 (2016) [[arXiv:1511.00132](#) [hep-ph]].

- [51] D. E. Kaplan and R. Rattazzi, “*Large field excursions and approximate discrete symmetries from a clockwork axion,*” *Phys. Rev. D* **93**, no. 8, 085007 (2016) [[arXiv:1511.01827](#) [hep-ph]].
- [52] N. S. Kardashev *et al.* [RadioAstron Collaboration], “*RadioAstron – a Telescope with a Size of 300 000 km: Main Parameters and First Observational Results,*” *Astronomy Reports* **57**, 153 (2013) [[arXiv:1303.5013](#) [astro-ph.IM]].
- [53] [RadioAstron website](#)
- [54] A. P. Lobanov *et al.*, “*RadioAstron space VLBI imaging of polarized radio emission in the high-redshift quasar 0642+449 at 1.6 GHz,*” *Astronomy and Astrophysics* **583** (2015), A100 [[arXiv:1504.04273](#) [astro-ph.GA]].
- [55] A. Payez, C. Evoli, T. Fischer, M. Giannotti, A. Mirizzi and A. Ringwald, “*Revisiting the SN1987A gamma-ray limit on ultralight axion-like particles,*” *JCAP* **1502**, no. 02, 006 (2015) [[arXiv:1410.3747](#) [astro-ph.HE]].
- [56] Y. Kahn, B. R. Safdi and J. Thaler, “*Broadband and Resonant Approaches to Axion Dark Matter Detection,*” *Phys. Rev. Lett.* **117**, no. 14, 141801 (2016) [[arXiv:1602.01086](#) [hep-ph]].
- [57] P. W. Graham and S. Rajendran, “*New Observables for Direct Detection of Axion Dark Matter,*” *Phys. Rev. D* **88**, 035023 (2013) [[arXiv:1306.6088](#) [hep-ph]].
- [58] H. Tashiro, J. Silk and D. J. E. Marsh, “*Constraints on primordial magnetic fields from CMB distortions in the axiverse,*” *Phys. Rev. D* **88**, no. 12, 125024 (2013) [[arXiv:1308.0314](#) [astro-ph.CO]].
- [59] P. Andre *et al.* [PRISM Collaboration], “*PRISM (Polarized Radiation Imaging and Spectroscopy Mission): A White Paper on the Ultimate Polarimetric Spectro-Imaging of the Microwave and Far-Infrared Sky,*” [arXiv:1306.2259](#) [astro-ph.CO].
- [60] M. Schlederer and G. Sigl, “*Constraining ALP-photon coupling using galaxy clusters,*” *JCAP* **1601**, no. 01, 038 (2016) [[arXiv:1507.02855](#) [hep-ph]].
- [61] P. A. R. Ade *et al.* [Planck Collaboration], “*Planck 2015 results. XIX. Constraints on primordial magnetic fields,*” *Astron. Astrophys.* **594**, A19 (2016) [[arXiv:1502.01594](#) [astro-ph.CO]].
- [62] B. F. Burke and F. Graham-Smith, “*An Introduction to Radio Astronomy,*” Cambridge University Press, 2010.
- [63] J. H. Taylor and J. M. Cordes, “*Pulsar distances and the galactic distribution of free electrons,*” *Astrophys. J.* **411**, 674 (1993).
- [64] J. W. Armstrong, B. J. Rickett and S. R. Spangler, “*Electron density power spectrum in the local interstellar medium,*” *Astrophys. J.* **443**, 209 (1995).
- [65] J. M. Cordes and T. J. W. Lazio, “*NE2001. 1. A New model for the galactic distribution of free electrons and its fluctuations,*” [astro-ph/0207156](#).
- [66] A. N. Hall and D. W. Sciama, “*The angular broadening of compact radio sources observed through ionized gas in a rich cluster of galaxies,*” *Apj.* **228**, L15-L18 (1979).

- [67] A. Ferrara and R. Perna, “*Scintillation as a probe of the intergalactic medium,*” *Mon. Not. Roy. Astron. Soc.* **325**, 1643 (2001) [[astro-ph/0104189](#)].
- [68] A. Pallottini, A. Ferrara and C. Evoli, “*Simulating intergalactic quasar scintillation,*” *Mon. Not. Roy. Astron. Soc.* **434**, 3293 (2013) [[arXiv:1307.2573](#) [astro-ph.CO]].
- [69] J. P. Macquart and J. Y. Koay, “*Temporal Smearing of Transient Radio Sources by the Intergalactic Medium,*” *Astrophys. J.* **776**, 125 (2013) [[arXiv:1308.4459](#) [astro-ph.CO]].
- [70] P. A. R. Ade *et al.* [Planck Collaboration], “*Planck 2015 results. XIII. Cosmological parameters,*” *Astron. Astrophys.* **594** (2016) A13 [[arXiv:1502.01589](#) [astro-ph.CO]].
- [71] B. P. Abbott *et al.* [LIGO Scientific and Virgo Collaborations], “*Observation of Gravitational Waves from a Binary Black Hole Merger,*” *Phys. Rev. Lett.* **116**, no. 6, 061102 (2016) [[arXiv:1602.03837](#) [gr-qc]].
- [72] E. W. Leaver, “*An Analytic representation for the quasi normal modes of Kerr black holes,*” *Proc. Roy. Soc. Lond. A* **402**, 285 (1985).
- [73] S. R. Dolan, “*Instability of the massive Klein-Gordon field on the Kerr spacetime,*” *Phys. Rev. D* **76**, 084001 (2007) [[arXiv:0705.2880](#) [gr-qc]].
- [74] P. Pani, *Int. J. Mod. Phys. A* **28**, 1340018 (2013) [[arXiv:1305.6759](#) [gr-qc]].